

Tunable infrared transmission for energy efficient pneumatic building façades

Lara Tomholt^{1,2*}, Olga Geletina¹, Jack Alvarenga², Anna V. Shneidman³, James C. Weaver²,
Matheus C. Fernandes^{2,3}, Santiago A. Mota^{1,3}, Martin Bechthold¹, Joanna Aizenberg^{2,3}

¹Harvard Graduate School of Design, 48 Quincy St., Cambridge, MA 02138, USA

²Wyss Institute for Biologically Inspired Engineering at Harvard University, 3 Blackfan Circle, Boston, MA 02115, USA

³John A. Paulson School of Engineering and Applied Sciences, Harvard University, Cambridge, MA 02138 USA

* Corresponding author; ltomholt@gsd.harvard.edu

ABSTRACT

Thermal regulation of buildings in climates with daily and seasonal weather changes can prove challenging and result in high building energy consumption. While adaptable façades with tunable infrared transmitting properties would be able to modulate solar transmittance through the building envelope and as such increase energy efficiency, available technologies are often expensive, relatively complicated, and challenging to implement in a lightweight form factor.

Motivated by these limitations, this report presents a novel tunable light-modulating technology for energy efficient pneumatic façades in the form of polydimethylsiloxane (PDMS) film with a thin gold surface coating. Sequential stretching and relaxing of this film results in strain-induced microscale surface cracks that can significantly modulate both visible and near infrared light transmission and consequently the material's solar heat gain coefficient (SHGC).

The material's tunability has shown a significant potential to reduce building energy use, as assessed with building simulation software. The technology offers additional advantages for light modulation in pneumatic façades including real-time operation, ease of implementation and control, and predictable performance. Façade design guidelines for the integration of the infrared regulating film into ethylene tetrafluoroethylene (ETFE) building envelopes and climate suitability are described, and a critical evaluation of material durability, optical clarity, and material costs are provided.

Keywords

Adaptable façades, tunable material, solar, near infrared regulation, pneumatic façades, PDMS (polydimethylsiloxane), ETFE (ethylene tetrafluoroethylene).

1. Introduction

1.1 Light modulating adaptable façades

Presently, as the building sector is generating approximately 40% of global carbon emissions [1], and the impacts of global climate change are accelerating [2], the necessity to reduce the carbon footprint of buildings has become ever more urgent. Approximately one third of global primary energy is used to heat, cool, illuminate, and ventilate buildings [1]. The building envelope plays a major role in managing building energy use, as it is responsible for regulating daylight, heat exchange, and solar gains, to name just a few factors. However, while the exterior environmental conditions change daily and seasonally, most building façades are designed as static layers, with reasonably good performance tailored to average environmental conditions at the expense of high energy loads.

Adaptable façades that configure their physical properties to external stimuli have long been considered a promising solution for energy efficient buildings [3–7], and researchers are exploring new and innovative responsive materials for that purpose, such as hygromorphic solar shading systems [8,9], phase change materials for latent heat storage [10-12], or shape memory materials to regulate infiltration rate [13,14]. A particular focus has been on the development of adaptive transparent systems in glazing and pneumatic envelopes [3,15-17] that can modulate heat flow through the building envelope and as such, block solar heat during warm periods and save on cooling energy but also exploit thermal gain from the sun during colder conditions to reduce energy consumption for heating. The requirements of these systems are challenging, as they have to negotiate the need for daylight access, with the dilemma of excessive glare or unwanted solar gains. Shading systems that reduce glare and solar heat gain can obstruct views of the outdoors, have negative health effects on building occupants [18-20], and increase energy consumption from artificial lighting. Adaptable shading elements can also be costly to install, tend to be mechanically elaborate, and lead to high maintenance costs [4,21].

Significant progress has been made in the development of glass with switchable optical properties (smart glazing) to modulate solar transmittance [15,22-25]. Chromic materials [26-29], liquid crystals [30-34], and suspended particle devices [35,36] have been developed over the last few decades, but these solutions remain costly [25,37], and require high levels of expertise and complicated processes to develop [25,38]. Many of these systems only switch between a small number of states [39,40] and response times can reach tens of minutes [28,38]. Though the technologies may be well suited to

regulate visible light transmittance, some show only a limited ability to modulate near-infrared light [23,41].

Kinetic motorized daylight control systems consisting of multiple interconnected components, such as blinds or adaptive fritting [42-44], can also be effective [45], but are typically quite complex, especially when targeting fast response times, and require regular maintenance [4,21,46,47]. In contrast, compliant systems with tunable materials [22,48] possessing carefully set light transmittive properties - such as the flexible films presented herein - hold great promise for innovative, scalable adaptable façade solutions with real-time responsiveness and ease of control. Compliancy becomes particularly imperative as architects are progressively adopting new, more sustainable types of envelopes for buildings, including lightweight membrane-based tensile structures and pneumatic façades [49].

1.2 ETFE façades

Ethylene tetrafluoroethylene (ETFE) [50] is a common synthetic membrane used for pneumatic roofing and façade solutions [16,51-53]. It is a relatively cost efficient façade material and extremely lightweight, thus reducing structural loads [54]. ETFE is UV resistant and transmits up to 95 percent of visible light [50,54-56]. Most systems feature pneumatic post-tensioning that involve pillow-like cushions of two or more film layers, which can provide high levels of thermal insulation (about 1.9 W/m²K for three-layer cushions) [57].

However, due to the material thinness and high optical transmittance across the near infrared wavelength range, clear ETFE film has a high solar heat gain coefficient (SHGC) [54], which increases the risk of overheating and can lead to excessive glare [58,59]. In response to these challenges, new ETFE products have been developed, such as heat absorbing ETFE film which saves on energy consumption for cooling during hot seasons, but also increases the heating energy demand during cold ones [60,61]. Another concept uses a millimeter-scale geometric modification of ETFE film that can effectively block direct solar radiation while allowing diffuse light to enter [62]. The limitation of these approaches is that the SHGC is fixed and cannot respond to changing exterior conditions.

A more adaptable shading technology is the active control of so-called “fritted” ETFE films with an offset pattern of highly reflective silver pigments [16,51-53]. It features three- or four-layer cushions of which two layers of fritted ETFE film that can be moved closer together (“closed”) or further apart (“open”) through pressure changes in the cavity between them [3,51,63]. When the layers

move close together, the superimposition of the two patterns reduces glare and heat gain, but when moved apart, the system allows more sunlight through. While this approach demonstrates promising differences in transmittance values [3], repositioning the fritted layer [51] limits the number of states the system can take on to just two (open and closed). Studies have also shown that the optical performance of these switchable ETFE cushions is highly dependent on the solar incidence angle in the open state [3], which can lead to inconsistent performance and consequently reduced building energy efficiency. Other problems include limitations on user comfort: the printed pattern blocks visible and near infrared light to the same extent (Figure S01) and obstructs views to the exterior (Figure S02).

1.3 Ambitions

The limitations of smart glazing and pneumatic shading technologies highlight the need for new materials with tunable optical performance. In order for them to be viable candidates for energy-efficient buildings, infrared regulating materials should be inexpensive, technologically simple, scalable, and allow for quick, precise and continuous modulation of infrared transmission, without compromising visible light transmittance and corresponding views to the exterior. The present report describes a new pneumatically actuated thin film material system that achieved these highly desired properties through the process of gold coating the well-established polymer polydimethylsiloxane (PDMS).

The objectives were to optimize the material performance according to the degree and tunable range of near-infrared transmission (Sections 3-5). The optimized material was compared to commercially available light regulating technologies and used to simulate building energy savings associated with its proposed implementation (Section 6). Subsequently, the material was evaluated on the quality of the view to the exterior (Section 7.1), and façade guidelines were developed for the integration of infrared regulating film into ETFE building envelopes (Section 7.2). Finally, the material cost (Section 7.3) and its durability were assessed (Section 7.4), and the climates for which pneumatic ETFE façades incorporating this new technology are suitable (Section 7.5) were identified.

2. Strain-dependent light regulation by PDMS films with surface modifications

Polydimethylsiloxane (PDMS) [64] is a silicone elastomer used in many areas of research and industry for a broad range of applications including soft lithography and microfluidic devices [65-67],

soft robotics [68], and flexible electronics [69-71]. As a cast film, the elastic properties (up to 100% elongation), high optical transparency [72], non-toxicity [64] and low cost (Section 7.3) of PDMS resemble the material characteristics of ETFE [50], albeit more pliable than ETFE, thus making it an ideal material to test new concepts and techniques for future adaptable façades. Several researchers have reported PDMS-based solutions for adaptable visible light regulation, including those containing fluidic channels [73,74], paraffin wax composites with thermally induced switching between transparent and opaque states [75], stretch-tunable polymer films incorporating micron-sized aluminum platelets [76], dyes [77], or nanoscale surface topographies [78].

An alternative and particularly promising route towards adaptable modulation of light transmission is to employ reversible wrinkling and cracking in thin rigid coatings (on the order of tens to several hundreds of nanometers [79-81]) on the surface of PDMS films. When the PDMS substrate is subject to a change in strain (due to mechanical stretching [79,82,83], thermal expansion [84,85], or solvent-induced swelling [86-88]), compressive stresses created through a Poisson-ratio effect across the thin film cause the stiff layer to crack and buckle into quasi-ordered arrays of micro-scale sinusoidal wrinkles [79,82,89,90]. The wrinkles can subsequently be reversibly flattened by returning the substrate to the strain at which the stiff overlayer was originally created. The amplitude of the wrinkles and size of the cracks is dependent on the thickness of the rigid surface coating and the applied strain [91-100], as has been demonstrated with a wide range of surface coatings, such as a thin layer of gold [101] or aluminum [102], or an oxidation-induced glass-like layer of silanol (SiOH) groups [79,82,99,100].

Controlled and reversible wrinkled and cracked surfaces have been investigated for many advanced applications [83,103-109], including light modulation approaches such as (sub)micron-sized PDMS pillar arrays atop the mechanically induced wrinkles [80] and bi-axial straining by pneumatic actuation of oxygen plasma-treated PDMS [99]. The micro-wrinkles and cracks on oxidized PDMS film scatter and diffuse light with applied strain, allowing for continuous control of visible light transmittance by switching the material between transparent and translucent states [79,99]. However, the scope of the previously mentioned studies on PDMS-based light modulation was limited to the visible light spectrum. The present work explores the performance of surface-modified PDMS membranes in the infrared spectrum and extends their applicability in tunable, heat flow regulating façades.

This study presents a novel application of strain-induced microscale wrinkling and cracking structures on gold coated PDMS films. The material's tunable surface morphology allows for significant

modulation of not only visible, but also near infrared light transmission. This technology offers advantages for light modulation in façades including real-time operation and ease of control.

3. Fabrication and actuation

3.1 Fabrication

The PDMS film used in these studies (Rogers Bisco HT-6240 [72], Rogers Corporation, Chandler, Arizona, USA) had a thickness of 250 μm and exhibited high optical clarity. Two sets of samples were prepared, each tailored to a different mode of mechanical actuation. The first was activated by a uniaxial strain (i.e. stretching and releasing the material at two opposite edges), which allowed for high-throughput testing. The other was actuated pneumatically, stretching the PDMS into a dome-like shape, analogous to the proposed actuation in pneumatic façades.

Samples for uniaxial actuation included PDMS films that were treated in their relaxed state (0% strain) or under strain (“pre-stretched” at 20% or 40% uniaxial strain), since the strain during treatment determines the microscale wrinkle amplitudes and frequencies on the film’s surface [79,80], and thus potential variation in visible and infrared light transmissive properties. The films were then oxygen plasma treated and/or sputter-coated with gold (Figure 1 and Supplemental Section 2.1). As a result of the findings presented in Section 4.2 the sample intended for pneumatic actuation was not pre-stretched and did not receive oxygen plasma treatment.

Since gold is environmentally stable (unlike other infrared reflective metals such as aluminum or other non-noble metals that run the risk of oxidizing quickly), it is a viable choice for façade applications. The thin gold coating has a thickness on the order of tens of nanometers as measured with atomic force microscopy (AFM) (Figure S03, Supplemental Section 2.1).

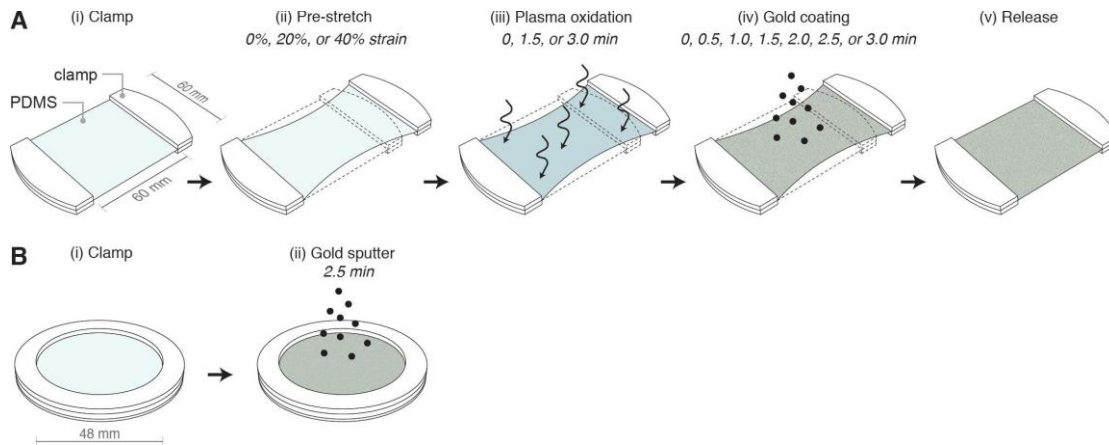


Figure 1 Fabrication sequence of infrared regulating PDMS film intended for uniaxial actuation (A) and pneumatic actuation (B).

3.2 Actuation

After fabrication, the uniaxial samples were subjected to strains of 0%, 20% and 40% for analysis of their optical transmission and microscopic surface characteristics. Each treated PDMS film was tightly secured between acrylic clamps at the edges perpendicular to the axis of actuation, and mounted on a custom fabricated acrylic fixture to ensure accurate strains for testing (Figure 2A). The pneumatic samples were actuated to 0%, 30% and 57% global strain (i.e. elongation of the cross-sectional arc length through the entire width of the sample) using a tube connected to an air supply that pressurizes the air chamber (Figure 2B, Supplemental Section 2.2). A 57% global strain curvature corresponded with a near-hemispherical geometry and was the maximum attainable curvature in the façade system proposed in this study. Due to the gas permeability of PDMS [64], actuation required a continuous low flow of air at a pressure of around 15 kPa (2 psi) to achieve 57% global strain. The speed of actuation between 0% and 57% global strain can be regulated by managing the pressure, but can be as fast as less than a second, thus allowing for real-time light tunability in a building envelope.

Pneumatic actuation of the PDMS caused variations in local strains on the film's surface, which in turn led to differences in optical transparency. In order to quantify those local strains Finite Element (FE) simulations of the PDMS was performed (Supplemental Section 2.3), which revealed appreciable differences in local in-plane logarithmic strain between surface points along the diameter d ($1/8d$, $1/4d$, $3/8d$, and $1/2d$) as global strain increased (Figure 2C, Figure S04 and Video 1).

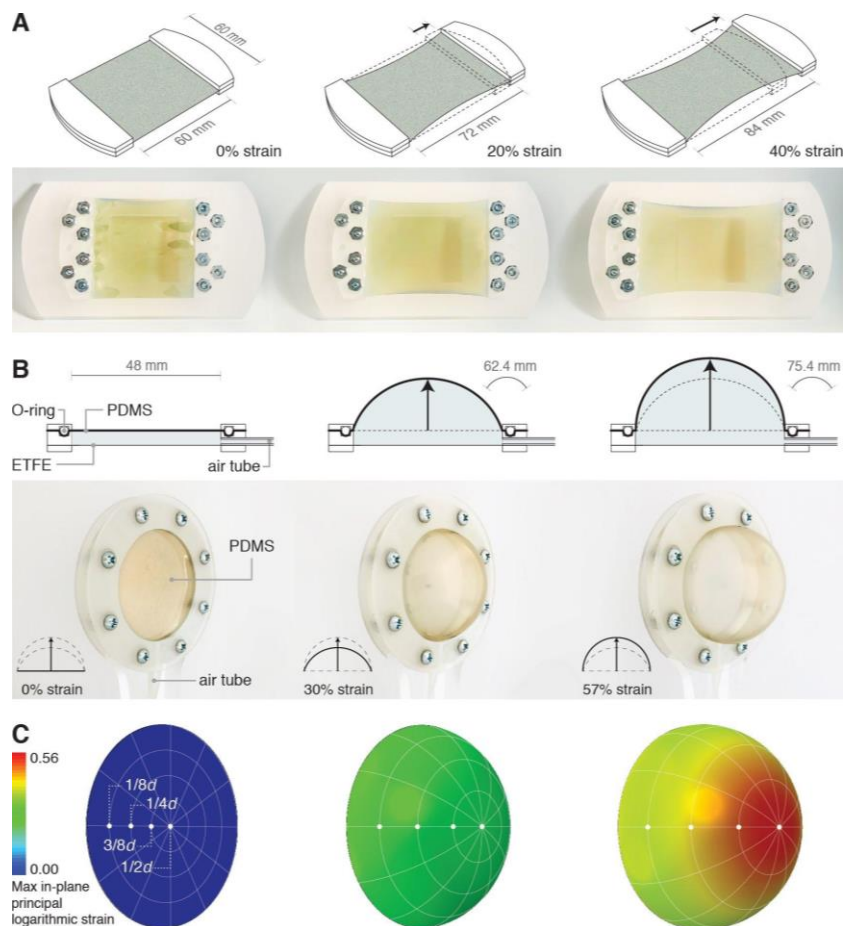


Figure 2 **Material actuation.** **A.** The uniaxial samples at 0%, 20% and 40% strain. The sample in the image was gold-coated for 2.5 minutes, without any pre-stretching or plasma oxidation. **B.** The pneumatic sample shown received the same treatment as in A. An acrylic assembly is used to clamp a treated PDMS film and ETFE sheet, enclosing an air chamber connected to an air supply. **C.** Finite Element simulations show that the maximum in-plane principal logarithmic strains experienced by the film are relatively similar for the points of interest ($1/8d$, $1/4d$, $3/8d$, $1/2d$) at 30% global strain, but become more distinct at larger global strains.

4. Infrared transmission and reflection performance

The samples were subsequently tested on their ability to regulate solar heat transmittance. Since solar irradiation intensity varies across the infrared spectrum (Supplemental Section 3.1, Figure S05), a weighted average of the materials' transmission ($T_{WA}\%$) and reflection over the 710 – 2600 nm near infrared radiation spectrum, using direct and circumsolar radiation intensities [110], gave the best indication of the material's total solar heat transmission and reflection. The film's overall visible light

transmission ($T_{VIS}\%$) was obtained by taking the average of the transmission values in the 380 - 700 nm range.

The three treatment parameters (pre-stretching strain, oxygen plasma treatment, and gold sputtering duration (Section 3.1)) were optimized to maximize the material's tunability range, that is, the range of infrared transmission ($\Delta T_{WA}\%$) or reflection upon uniaxial actuation of the sample between 0% and 40% strain. After all, in cases of more extreme hot and cold weather, a façade with a greater range of infrared tunability can more closely approach the optimum transmission value to minimize building energy consumption year-round. Spectrophotometric analysis (Supplemental Section 3.2) first showed high visible light transmissions relative to the rest of the spectrum (discernable in the peak around 500 nm) for all of the treated samples and imposed actuation strains (Figure 3A and Figure S06), which would be considered a desirable material attribute in a building façade. As shown in Figure 3B, the tunable infrared transmission range increased with a lower pre-stretched strain during treatment and by eliminating oxygen plasma exposure from the sequence of treatments. These results also demonstrated that the tunability range and gold sputtering time are positively correlated (Figure 3B and Figure S07). Within this study's collection of treatments, the greatest tunable range ($\Delta T_{WA}\%$ of 26.5%) was achieved with a gold sputtering time of 2.5 min (corresponding to a 25 nm thickness) without pre-stretching or plasma oxidation (Figure 3C), which could be increased up to a $\Delta T_{WA}\%$ of at least 37.9% when actuated beyond 40% strain (Figure S08). This treatment was therefore used for subsequent prototyping studies.

Next, the infrared tunability was assessed for pneumatically actuated PDMS film with this treatment. Since local strains, as demonstrated with FE simulations (Figure 2C), were zero across the entire surface at 0% global strain, light transmission and reflection at points across the surface have similar values. At 57% global strain, the local strains become more varied and consequently the differences in transmission and reflection values between the three points of interest ($1/4d$, $3/8d$ and $1/2d$) become more pronounced (Figure 3D and Figure S09A). The measured transmission values and the simulated local strains show a direct correlation (Figure 3E and Figure S09B). The overall surface of the pneumatically actuated film was estimated to reach a $\Delta T_{WA}\%$ of 32.4% between 0% ($T_{WA}\%$ of 13.2%) and 57% ($T_{WA}\%$ of 45.6%) global strain (Figure 3F, Supplemental Section 3.4, Figure S09C).

The infrared transmitting properties of both uniaxial and pneumatic samples showed full reversibility upon repeated actuation. In addition, preliminary tests suggest that optical performance is

largely independent from the light's angle of incidence (Figure S10), which is a beneficial characteristic as it allows for reliable tuning of infrared transmission, regardless of the sun's position.

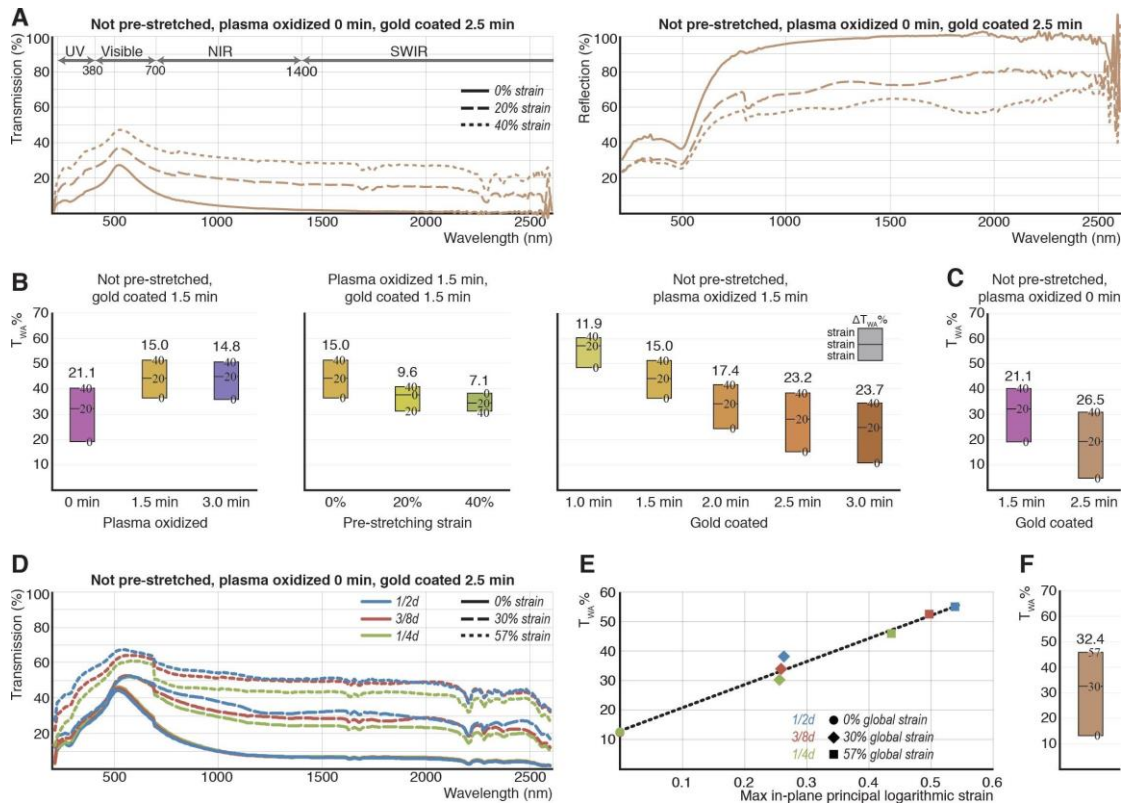


Figure 3 *Transmittance and reflection in the visible and near infrared light spectrum. A.* Treatment of the sample in a relaxed state results in lowest optical transmission at 0% strain, with an increase in transmission upon uniaxial actuation. An increased gap between the data curves of 0% strain and the maximum strain is associated with an increased adaptability. **B.** Plots of weighted averages of infrared transmission (710 – 2600 nm) through uniaxially strained samples. Colors represent the different treatments, and are equivalent to those in Figure S06 and S12. **C.** The uniaxially actuated samples with the highest adaptability in infrared transmission had received treatment in an unstrained state and were not exposed to oxygen plasma. Matching the trend seen in (B), a thicker layer of gold enhances adaptability. **D.** Transmission values for a pneumatically actuated film measured at the three points of interest (1/4d, 3/8d and 1/2d). **E.** The $T_{WA}\%$ of the sample in (D) and local strains at different points of interest on the surface show a linear correlation. **F.** Plot of weighted averages for infrared transmission (710 – 2600 nm) through the pneumatically actuated sample.

To support these single-point spectrophotometry measurements and to give an indication of the ability of the adaptable technology to regulate the interior temperature of an enclosed environment, the

performance of the entire sample surface was evaluated in an experimental setup with an insulated box and heat lamp (Supplemental Section 5, Figure S16). Enclosing the box with 2.5 min gold coated PDMS film at 0% strain resulted in a reduced steady state temperature of the enclosed space and an increased timeframe to reach that temperature compared to enclosing the box with the material at 40% strain, confirming the trends observed with spectrophotometry analysis (Supplemental Section 5.2, Figure S17).

5. Microscale surface characteristics and infrared transmission

The microscale wrinkles and cracks appearing on the film's surface were characterized by optical (Figure 4, Figure S11, Figure S12 and Figure S15), atomic force (Figure S13), and scanning electron microscopy (Figure S14).

Uniaxial actuation results in the formation of linear wrinkles as a result of Poisson compression (Figure 4A and Figure S11). The direction of the observed wrinkles with respect to the axis of pull agreed well with wrinkling and cracking trends demonstrated in preceding studies [79,99,100]. Simultaneously, it was revealed that the cracks widen with an increase in tensile stresses in the plasma-treated and/or gold-coated layer of uniaxially actuated film [95]. The thicker the rigid layer (as a result of increased oxidation and/or gold deposition time), the wider the cracks generated upon stretching or releasing the film away from the treatment strain (Figure 4A and Figure S12).

The overviews presented in Figure 4A and Figure S11 also show that infrared transmission during sample actuation increases with a corresponding increase in crack widths. The PDMS treatment resulting in the greatest $\Delta T_{WA}\%$ upon uniaxial actuation (gold coated for 2.5 minutes without pre-stretching or plasma oxidation, see Figure 3C) also displays the biggest change in crack widths (from 0.6 to 5.5 μm between 0% and 40% strain, respectively) (Figure 4A). Surface analyses (Supplemental Section 4.1) confirmed a positive linear correlation between the material's strain dependent infrared transmission and crack surface area, suggesting infrared light is primarily transmitted through cracks in the top rigid surface and transmission is regulated by the extent of crack formation (Figure 4A, Figure S12).

Upon pneumatic actuation, the gold coated PDMS films did not experience compressive forces, and, consequently, did not exhibit any wrinkling morphologies (Figure 4B). Surface cracks in

pneumatically actuated gold coated PDMS films form in an island-like pattern over the entire film surface [99], generating a higher crack surface area upon actuation (Figure 4B, Figure S15) than in uniaxially actuated samples. Due to the absence of wrinkle formations on the surface, reversible crack formations on the surface are thus confirmed to be responsible for the bulk change in transmission of infrared energy upon actuation.

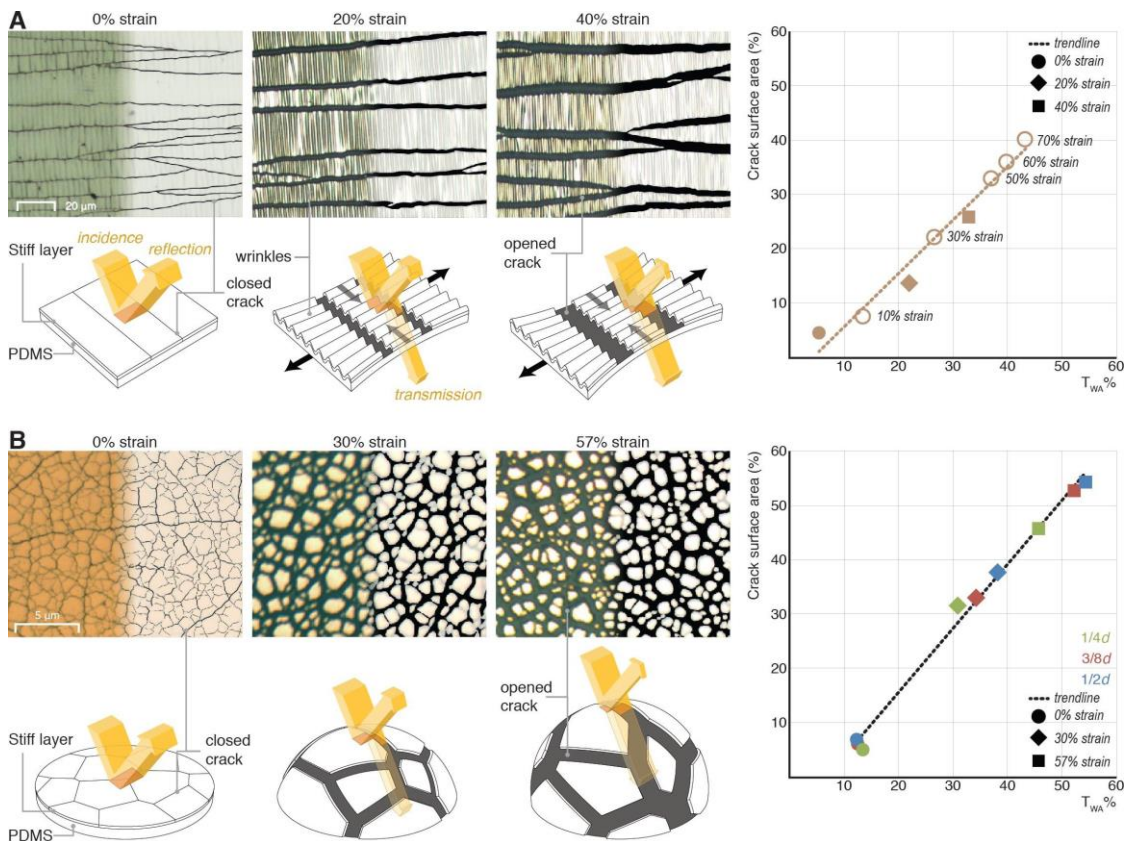


Figure 4 Composite optical microscopy images (left: raw image; right: processed image) of the top rigid layer of the PDMS (gold sputtered for 2.5 min without pre-stretching or plasma oxidation) reveal straight wrinkle and crack patterns in uniaxially strained samples (A) and island-like crack patterns without wrinkles in pneumatically actuated film (B). The correlations between crack surface area and infrared transmission suggest infrared light transmission is regulated by the extent of crack formation as visualized in the diagrams below.

6. Building energy savings analysis

6.1 U-value and adaptable SHGC

The thermal performance of a window or other transparent façade element is determined by two main ratings: the Solar Heat Gain Coefficient (SHGC) and the thermal transmittance (U-value). The SHGC is defined as the fraction of incident solar radiation that travels through the material as heat gain. A lower SHGC means a lower solar transmission and heat gain. The U-value of a building element is a measure of thermal transmittance in units of W/m²K. All SHGCs and U-values calculated and presented here are “center-of-glass” values. For adaptable windows to have the largest impact on building energy efficiency in climates with seasonal temperature variation (Section 7.5), they need to be able to achieve a low SHGC during hot (summer) days to reflect solar heat, and a high SHGC in cold (winter) periods to allow for passive solar gain. This study therefore had the ultimate goal of identifying material surface treatments that achieve the greatest range (delta) in SHGC upon actuation of the PDMS film, as visualized in Figure 5A.

The SHGC of a single layer material can be calculated with its transmission (τ), absorption (α), and inward flowing fraction (N_i) of the absorbed infrared with Eq. (1) [111,112]:

$$(1) \quad SHGC = \tau + N_i * \alpha$$

The absorption coefficient (α) of this study’s new material was inferred according to the conservation of energy Eq. (2) which requires that a material’s transmittance coefficient (τ), reflection coefficient (ρ) and absorption coefficient (α) add up to 1:

$$(2) \quad 1 = \tau + \alpha + \rho$$

Following Eq. (1) and (2), using the measured weighted average values for transmission and reflection (Section 4.2) and an assumed value for the inward flowing fraction N_i of 0.5, pneumatically actuated, gold coated PDMS film was estimated to achieve a Δ SHGC of 0.34 when actuated between 0% and 57% global strain (SHGC of 0.21 and 0.55, respectively). When integrated in a double layer clear ETFE cushion, the SHGC of the whole façade assembly can be obtained by multiplying the SHGC of the treated PDMS with the SHGC of a two-layer ETFE cushion ($0.925^2 = 0.86$) [54]. Visible light transmission values were obtained in the same manner with a T_{VIS} of the two-layer ETFE cushion of 0.86 (0.925^2) [54]. Following this methodology, the complete pneumatic façade system consisting of

two layers of clear ETFE and one layer of treated PDMS film is estimated to achieve a Δ SHGC of 0.29 (Figure 65B). Based on the specific solar intensities of that relate to a building's climate conditions and façade orientations, variations in gold sputtering duration can be optimized to suit many desired ranges of SHGCs.

The U-value of gold coated PDMS film can be calculated using Eq. (3), based on the formulas for thermal resistance R and thermal transmittance U :

$$(3) \quad U = \frac{1}{\frac{l_{\text{PDMS}}}{\lambda_{\text{PDMS}}} + \frac{l_{\text{Au}}}{\lambda_{\text{Au}}}}$$

with thermal conductivity (λ) and layer thickness (l) of the material's components. Standard clear ETFE for façade application has a thickness in the range of 100-300 μm [113] and a thermal conductivity of around 0.17 W/mK, both comparable with the PDMS used in this study (250 μm and 0.15 W/mK [64]). For the purposes of building energy simulation, the similarity of these values, in addition to the fact that the gold layer deposited on the PDMS film is very thin (on the order of tens of nanometers) and will have a negligible impact on the film's overall U-value conforming Eq. (3), an approximated U-value of 1.9 W/m²K for a three-layer ETFE/PDMS cushion was used, equal to a typical three-layer clear ETFE cushion [57].

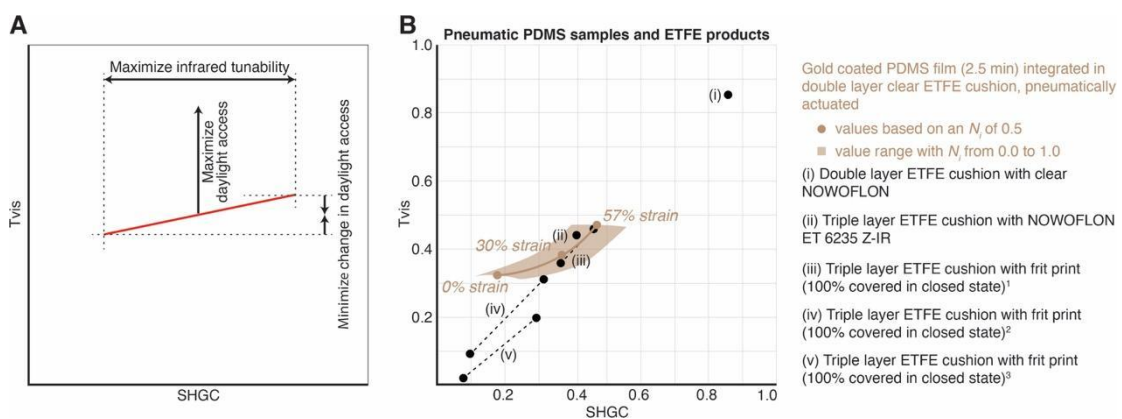


Figure 5—A. Illustration of this study's goal for the visible light transmission and SHGC performance of the infrared regulating PDMS film. B. SHGC and visual light transmittance of an ETFE façade assembly with gold treated PDMS film (brown) compared with existing technologies (black). Gold sputtered PDMS films can be continuously stretched to any desired strain between 0% and the

maximum strain (continuous line) and thus offer more adaptability than façades with fritted ETFE or infrared absorbing ETFE that take on just two states (dotted line), and one state, respectively. Frit print data obtained from [3]: ¹ frit print 3, ² frit print 1, ³ frit print 8. ETFE cushion data calculated or taken from [54, 60].

6.2 Simulation setup

The effects of the presented PDMS-based adaptable technology on building energy consumption were evaluated using DesignBuilder (DesignBuilder Software Limited, Gloucestershire, UK), a graphical user interface for the building energy simulation tool EnergyPlus (U.S. Department of Energy and National Renewable Energy Laboratory, USA). The effects of a façade assembly of two layers of ETFE and one layer of gold-coated (2.5 minutes) PDMS film on building energy use were compared to those with triple-layer clear ETFE cushions and triple-layer ETFE cushions of which one layer is a commercially available infrared absorbing ETFE layer, hereinafter referred to as “with treated PDMS film”, “clear”, and “with Z-IR film”, respectively. In addition, the simulation provided an indication of how frequently the actuation strain of the PDMS film is expected to change in order to provide the most efficient SHGC.

A single room with a south-facing ETFE façade was set to maintain an indoor temperature between 20 °C and 22 °C (Figure 6A, Table 1). The simulation was performed with weather data from Boston, MA, USA, which is known for its warm summers and cold winters and is therefore an ideal test site to ascertain the building energy savings potential of the façade’s tunability. Simulation parameters and façade properties are detailed in Table 1 and 2.

Simulation parameter	Setting	
Zone volume	974 m ³	
Zone floor area	162.33 m ²	
Construction adjacency (Floor, ceiling, all walls except ETFE façade)	Adiabatic	
Ventilation	Mechanical ventilation with heating and cooling, infiltration rate of 10 L/s - person	
Heating and cooling operation	Seasonal control	All year, 5 days/week
	Heating temperature	20.0 °C
	Heating setpoint	19.0 °C
	Cooling temperature	22.0 °C
	Cooling setpoint	23.0 °C
Activity	Template	Eating/drinking area
	Occupancy	0.2062 people/m ² , 5 days/week

	Equipment heat gain	0 W/m ²
Lighting	General lighting	5.0 W/m ² , 100 lux
	Target illuminance	250 lux

Table 1 Building model and parameter settings used in the building energy simulation

Despite recent developments of adaptive façade technologies, a common framework to assess their performance with building energy simulations is lacking, and as such, researchers use a wide variety of simulation and optimization methods [29,114,115]. For the performance assessment of this study's tunable pneumatic façade with gold coated PDMS film, multiple simulations were run for one year with a one-hour time step, with each simulation featuring one of the above mentioned façade assemblies selected for the south façade (Table 2). The simulations for the ETFE cushion with PDMS film were executed individually for each strain of the PDMS film (between 0% and 57% in increments of 5%). Subsequently, for each hour, the strain providing the lowest energy consumption for heating and cooling was selected (favoring strains closest to 0%), and the total yearly energy consumption calculated. Thermal inertia effects of the gold coated PDMS film were disregarded on the basis of the relatively low absorptivity of the material system for all applied actuation strains (Section 4.2).

Façade assembly	Strain (%)	SHGC	T _{vis}	U-value (W/m ² K)
Triple-layer clear ETFE cushion ¹		0.75	0.71	1.9 ³
Triple-layer ETFE cushion with 2 layers of clear ETFE and one layer of infrared absorbing film ²		0.41	0.44	1.9
Triple-layer cushion with 2 layers of clear ETFE and one layer of treated PDMS film (gold coated for 2.5 minutes without pre-stretching or plasma oxidation), with PDMS film at strain (%).	0	0.18	0.32	1.9
	5	0.21	0.33	1.9
	10	0.24	0.34	1.9
	15	0.27	0.35	1.9
	20	0.30	0.36	1.9
	25	0.34	0.37	1.9
	30	0.37	0.38	1.9
	35	0.38	0.40	1.9
	40	0.40	0.41	1.9
	45	0.42	0.43	1.9
	50	0.44	0.44	1.9
	55	0.46	0.46	1.9
	57	0.47	0.47	1.9

Table 2 Optical and thermal properties of the three types of ETFE façade assemblies used in the building energy simulation. ¹Data obtained from [60]; ²Data obtained from [60]; ³Data obtained from [57]. The SHGC and T_{vis} of the façade assembly with treated PDMS film was calculated for actuation

strains 0%, 30% and 57%, based on spectrophotometry data. These values were interpolated to estimate the other actuation strains.

6.3 Energy savings for heating and cooling

The simulations showed that this new adaptable façade technology can significantly reduce building energy consumption for heating and cooling: a 70% reduction compared to a clear ETFE façade and a 41% decrease compared to a façade with infrared absorbing ETFE (Figure 6B). As would be expected, compared to the clear ETFE assembly, both the infrared absorbing ETFE façade and the ETFE façade with gold coated PDMS allow for less solar gain during heating hours due to their lower SHGC values (Figure 6C), and consequently increase energy consumption for heating (Figure 6B). However, the adaptable nature of the PDMS façade allows for both higher and lower solar gains than the façade with infrared absorbing ETFE (Figure S18A), which comparatively, decreases both the energy consumption for heating and for cooling. The simulations revealed just small increases for artificial lighting for a building with an ETFE façade assembly with gold coated PDMS compared to one with a clear ETFE façade (5.8%) and with the infrared absorbing ETFE façade (1.7%).

While the PDMS film would be maintained at 0% global strain throughout most of the summer, during the rest of the seasons, the actuation strain would often be adjusted on an hourly basis (Figure 6D and Figure S18B). On many days the system would take advantage of the full tunability range, i.e. actuating the material between 0% and 57% global strain.

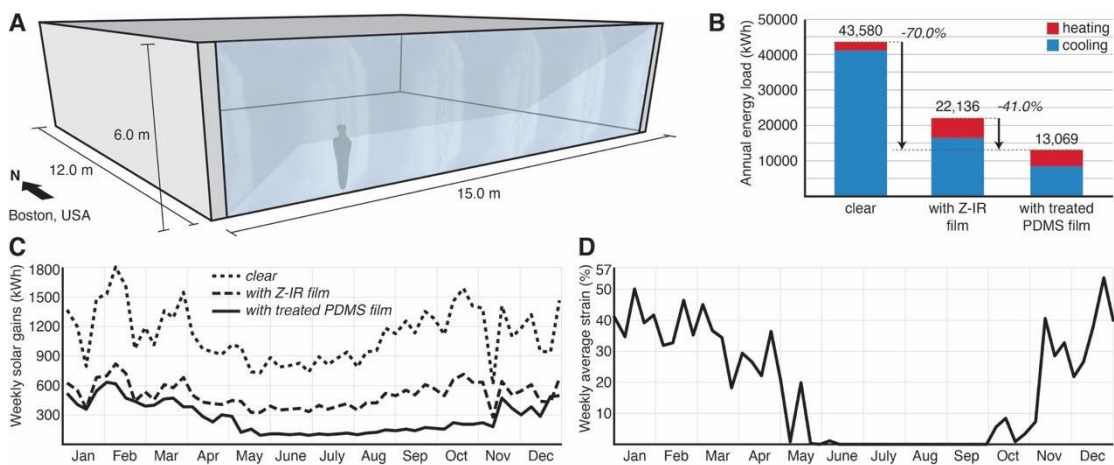


Figure 6 Building energy simulation model and performance. **A.** The simulation was performed on a single room with a south-facing ETFE façade. **B.** The simulation shows a significantly

reduced annual energy consumption for a façade assembly with adaptable gold coated PDMS film (2.5 min). C. Energy efficiency improvements for a façade with tunable PDMS film are the result of both an overall reduction in solar gains; and the ability to reach higher and lower solar gains than the static infrared absorbing material when necessary. D. The weekly average of the most efficient PDMS actuation strains (between 6 AM and 8 PM).

Since ETFE cushions are maintained at a very low internal pressure, typically between 200 and 600 Pa [3,116,117], the energy required for inflation is also very low, on the order of less than 1 kW/h for a medium sized façade [118, 119]. A potential increase in energy consumption for continuous pressure changes to actuate the PDMS film could therefore be well justified.

7. Building application considerations

7.1 View to the outdoors

Since windows that provide views to the outdoors, and in particular, views of greenspaces, can increase building occupants' psychological and physiological well-being [120, 121], the optical clarity of the new material system was evaluated. The material is tinted at 0% strain and becomes lighter upon uniaxial or pneumatic actuation. In contrast with uniaxially actuated gold-coated PDMS films that distort the view with increased strain (Figure S19), pneumatically actuated gold-coated PDMS films maintain acceptable optical clarity at any actuation strain (Figure 7, Video 2), potentially due to the absence of surface wrinkles. At larger actuation strains the material's curvature and microscale cracks cause slight changes in color and fading towards the edges of the film. This technology's ability to regulate infrared transmission but maintain a clear view to the out-of-doors is highly advantageous in building façades, and is only achieved to a limited extent in fritted ETFE films. (Figure S02).

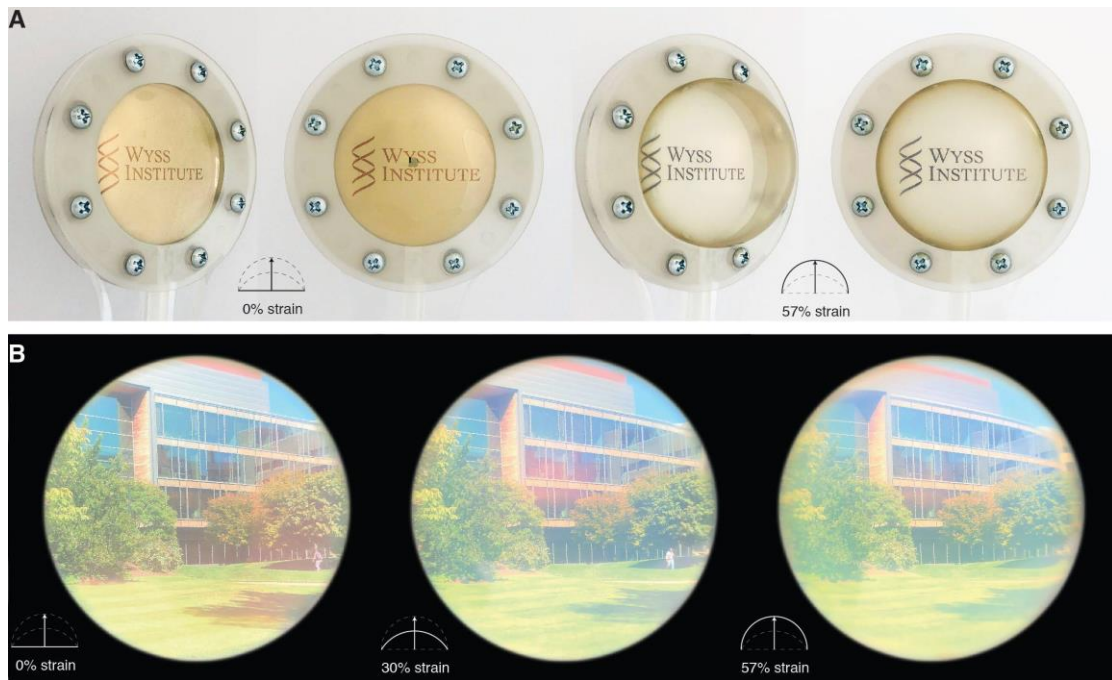


Figure 7 **A.** Treated PDMS film (gold coated for 2.5 minutes without pre-stretching or plasma oxidation) photographed with the treated side of the material facing the camera. **B.** The same PDMS film photographed with the treated side of the material facing the outdoors.

7.2 Scalability and manufacturing

Material costs for this new technology are low, making it ideally suited for large façades. The PDMS film used in this series of studies has a retail price of \$15 per ft² (\$161 per m²). With the current cost of gold at \$45 per gram and a film thickness of 25 nm (Figure S03) the gold surface coating would amount to \$2 per ft² (\$23 per m²) of treated surface area.

The low-e glass coating industry uses Magnetron Sputter Vacuum Deposition (MSVD) processes that coats glass with metals or metal oxides in vacuum chambers [122], analogous to the process used in this study. Since manufacturing technologies are already available and material costs are low, costs saved by reduced building energy consumption (Section 6) are expected to outweigh product costs for this novel technology.

7.3 Durability

With anticipated frequent and real-time actuation in a façade system, consistent mechanical and thermal performance of this infrared regulating technology is essential to ensure longevity and consistency in optical performance. To evaluate the durability of the gold coated PDMS, the sample was

continuously actuated uniaxially between 0% and 57% strain for 10,000 cycles and subsequently re-examined for its performance on infrared transmission (Supplemental Section 7.2, Figure S20A). The actuation strain of 57% represents the maximum material elongation for pneumatically actuated films explored in this study.

Infrared transmission changed insignificantly after continuous cyclical straining, with recorded changes potentially caused by the formation of additional cracks or partial delamination, as well as experimental variability (Figure S20B). Moreover, after 10,000 cycles, the material showed negligible deterioration in strength, with a mere 2.8% reduction in applied load to stretch the PDMS film to 57% strain, which can, in part, be accounted for by slight slipping of the sample in the experimental setup (Figure S20C). These results are in line with the reputation of PDMS providing long-term mechanical stability [64].

To add to its list of beneficial features for application in building façades, PDMS rubbers have demonstrated excellent resistance to ozone [123], UV light [64,124] and moisture [64]. Additionally, PDMS is inherently flame-resistant with autoignition temperatures of approximately 430°C [125]. In the event of a fire, generated silicon dioxide is not flammable, and gases formed are non-corrosive and non-toxic [125].

7.4 Façade integration

The presented, infrared-regulating gold-coated PDMS films can be easily integrated into ETFE façade systems both during new construction and as a retrofit. Within existing façade assemblies, ETFE cushions with two chambers each have their own air supply, allowing for pressure differentials between the chambers. The air valves are injection-molded into the ETFE and are connected with flexible tubes to the air distribution system [16,126] that provides the cushion with a constant air pressure. The internal pressure of an ETFE cushion is continuously regulated to compensate for air losses and exterior pressure fluctuations.

The infrared-regulating PDMS film is simply applied as a third layer between two outer ETFE layers. The control system for pneumatic actuation of the PDMS film would be connected to the air supply infrastructure already in place for the ETFE cushions.

The primary challenge in the integration of the PDMS films in ETFE façades is the need to reach large strains to achieve a high differential in infrared transmittive properties. Within a typical

three-layer ETFE façade cushion (with a width to height ratio of 1:2), the ETFE film cross-sectional curvature is up to 8% longer than its shortest span (width) and 2% longer than its largest span (height) [3,51], which limits the actuation of the interior PDMS layer to strains that have proven to be insufficient in effectively regulating infrared transmission (Figure 8A). In the proposed design, the PDMS sheet is compartmentalized by placing a “wire mesh” (or cable net) on top. The implementation of cable net structures in pneumatic ETFE façade assemblies is not uncommon [16,51]. A slim, flexible, but inextensible cable mesh tightly spanned and positioned on top of the PDMS sheet could be secured in place along with the ETFE and PDMS films in the edge clamps in the standard façade assembly structure. Upon pressurizing the bottom chamber, the smaller PDMS segments would be able to reach strains of 57% upon actuation (Figure 8B). With ETFE cushions increasing in thickness towards their center, polygon dimensions in the mesh can increase and generate PDMS curvatures with identical strains towards the center and thus minimize view obstruction by the mesh wire and increase the effective area of the PDMS sheet (Figure 8C). The tensile strength of the wire mesh would also provide a means to secure the position of the valve for the upper cushion chamber.

After assembly, the PDMS can be actuated automatically and in real-time by means of a computerized control system with light intensity and temperature sensors fixed on the façade’s exterior, similar to those already implemented in some fritted ETFE façades [127,128]. If the solar intensity is high and the indoor temperature rises above the upper threshold of the thermal comfort zone, the pressure in the bottom pillow chamber can be lowered to reduce the strain in the PDMS film and block more incoming infrared light. Conversely, when the indoor temperature drops below the lower threshold, the pressure is increased, allowing for more solar transmission through the PDMS layer enabling solar gain (Figure 8D, Video 3). This closed-loop façade system could be enhanced further, for example through integration with a building’s centralized control system and enhancement with optimization algorithms that are capable of learning from weather and indoor activity patterns, to proactively anticipate the most efficient actuation strain for building energy use and thermal comfort [129,130].

The smart integrated façade system and its rapid actuation allows the proposed façade assembly to accommodate for seasonal, daily, hourly, and even real-time changes in solar intensity, exterior temperature, and internal heat gain. Each façade section, and potentially each individual cushion, can be independently regulated based on differences in received solar heat as a result of the sun’s changing

azimuth and altitude, and local microclimates. In doing so, the building envelope would engage with its ever-changing environment, appearing almost “alive”.

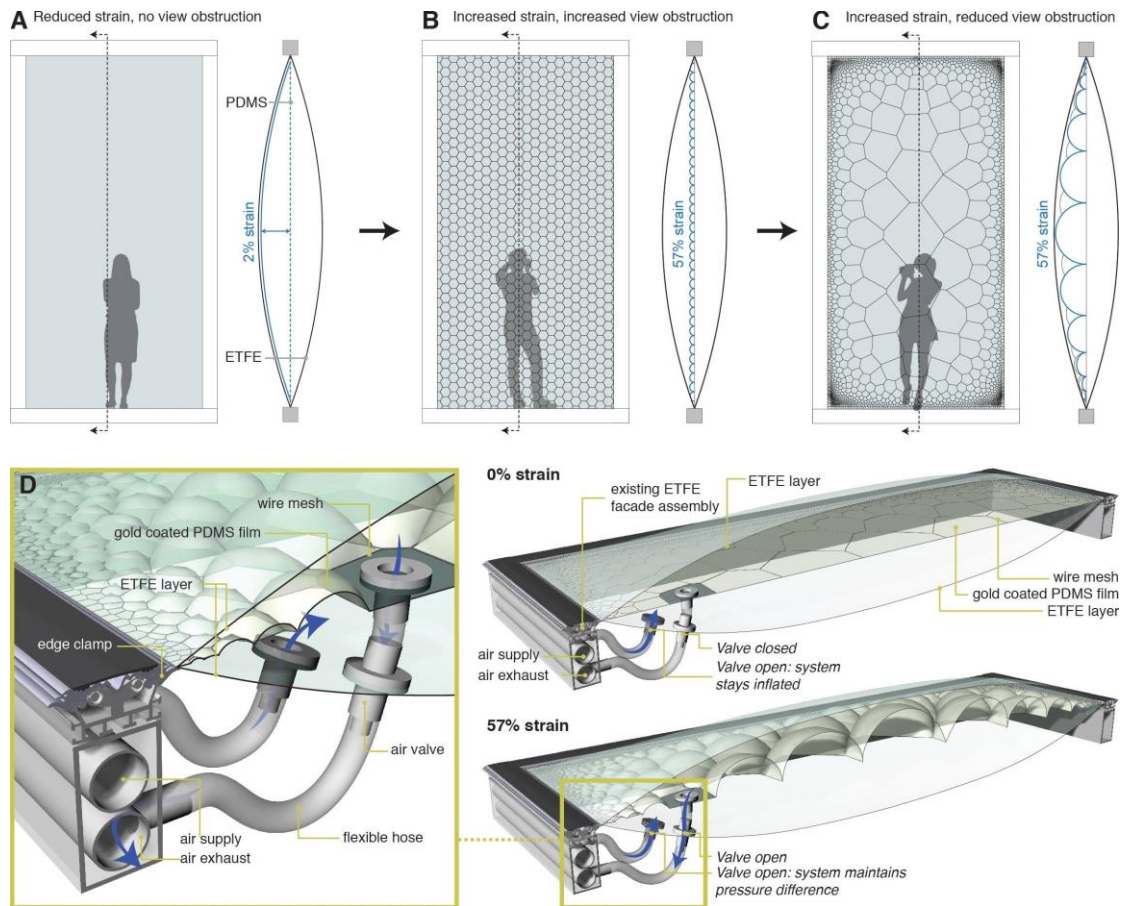


Figure 8 A. For a façade element with a typical ETFE cushion geometry, the maximum PDMS actuation strains would be insufficient to effectively regulate infrared transmission. B. A mesh-like net structure on top of the PDMS-creates smaller segments that can reach global strains of 57%. C. The curvature of the ETFE cushion allows PDMS sections to be larger towards the center of the cushion, which in turn, reduces potential view obstruction by the mesh compared with (B). D. Proposed integration and actuation of infrared regulating PDMS film in an ETFE façade system.

7.5 Target climates for façade application

Since the amount of gold sputtered on the material can easily be varied, the presented infrared-regulating façade technology can be tailored to multiple climate zones and microclimates. The most significant energy savings for heating and cooling can be expected in climates with large daily and/or seasonal temperature swings, in particular those with temperatures both above and below the comfortable indoor temperature of about 22°C (71.6°F). Following the Köppen climate classification [131], these temperature variations are common in the humid subtropical climate (Cfa), hot-summer Mediterranean climate (Csa) and hot-summer humid continental climate (Dfa), which can be found

across the globe and include many large cities such as Sydney, Australia; São Paulo, Brazil; Shanghai, China; and Toronto, Canada.

Presently, approximately 84% of ETFE façades are built in temperate humid or marine climates (Cf) [49,132]. However, the application of infrared-regulating PDMS films can make ETFE façades viable in climate zones previously considered unsuitable. The material's tunability also provides the potential for the façade to evolve along with changes in weather patterns as temperature swings become more pronounced and unpredictable [133].

8. Conclusion

The study has demonstrated that a material comprised of a PDMS elastomer with gold coating can significantly tune near infrared transmission. UV-Vis-NIR spectrophotometry analysis, Finite Element simulations, custom hotbox experiments, and optical microscopy have provided a complete picture of the impact of treatment and actuation strain on infrared transmission and the microscale surface cracks responsible for this behavior. The highest levels of infrared tunability were obtained by gold coating the PDMS films in an unstrained state for 2.5 minutes (corresponding to 25 nm thickness), without an additional plasma oxidation step. The effects of these treatments were explained by the positive correlation between the crack surface area and optical transmission upon actuation of the material.

Among the technology's most compelling advantages for implementation in pneumatic building façades are its full reversibility, scalability, easy actuation with a rapid response time of less than a second, substantial SHGC range of 0.34, while continuously providing a clear view to the exterior. Its fabrication and implementation in existing ETFE façade structures is straightforward and inexpensive. This study has shown that this new adaptable material can considerably reduce building energy loads for heating and cooling, outperforming non-adaptable ETFE technologies.

The research demonstrates that the new material system promises to be robust and maintain its optical performance after thousands of cycles. Further research is needed to determine its applicability for façades that typically have life spans on the order of 20-25 years. While the PDMS used in this series of studies was the most suitable choice for this research, the use of custom tailored, more mechanically robust PDMS films or elastomers with a lower level of viscoelasticity might prove more suitable for building deployment, considering the high temperatures façades can experience. Moreover, other

coating materials should be explored (other metals or metal oxides instead of gold, as well as surface primers or finishes), potentially leading to improved optical performance. In addition, pneumatic actuation was considered the most sensible actuation strategy for pneumatic ETFE façades, nevertheless, different actuation mechanisms should be explored (e.g. bi-axial actuation, iris mechanism), which might generate higher (local) strains and thus further expand the SHGC range.

In addition to the tunability of visible light and infrared in the solar spectrum, future studies investigating the material's performance on mid and long wavelength infrared light (heat radiation emitted by people and objects) would also be valuable in determining other roles the technology could play in façades, such as heat retention and/or night cooling. Preliminary tests performed in this study indicated an ability to regulate infrared light with longer wavelengths and a recent study has shown a polymer with a metal coating to successfully regulate long wavelength infrared transmission [134]. Moreover, the technology is amenable to other environments and scales that are attractive candidates for adaptability and self-regulation.

This paper provides one more example of how the interface between science and design can provide new concepts for energy-efficient façades. The novel film technology has shown the ability to contribute to energy savings in the built environment by responding to daily weather changes and the cycle of the seasons. Its tunability creates the opportunity to build ETFE façades in climates previously considered unsuitable and can help alleviate environmental consequences associated with climate change.

Acknowledgments

This research did not receive any specific grant from funding agencies in the public, commercial, or not-for-profit sectors. The work was performed in part at Harvard University's Center for Nanoscale Systems (CNS), a member of the National Nanotechnology Coordinated Infrastructure Network (NNCI), which is supported by the National Science Foundation under NSF award no. 1541959. The authors gratefully acknowledge the help received from Arthur McClelland, Grant T. England, Holly Samuelson, Jonathan Grinham, Ben Freedman, and Ali Malkawi.

Appendix A. Supplementary data

- Supplementary document containing additional documentation, including Figures S01 through S20.
- Video 1 – localized strain upon pneumatic actuation of PDMS film
- Video 2 – views through pneumatically actuated gold coated PDMS film
- Video 3 – proposal façade integration

References

- [1] UN Environment and International Energy Agency, 2018 Global Status Report: Towards a zero-emission, efficient and resilient buildings and construction sector, n.d. https://wedocs.unep.org/bitstream/handle/20.500.11822/27140/Global_Status_2018.pdf?sequence=1&isAllowed=y (accessed May 19, 2019).
- [2] WMO Statement on the State of the Global Climate in 2018, n.d. https://library.wmo.int/doc_num.php?explnum_id=5789 (accessed May 19, 2019).
- [3] J.-F. Flor, D. Liu, Y. Sun, P. Beccarelli, J. Chilton, Y. Wu, Optical aspects and energy performance of switchable ethylene-tetrafluoroethylene (ETFE) foil cushions, *Applied Energy*. 229 (n.d.) 335–351. doi:[10.1016/j.apenergy.2018.07.046](https://doi.org/10.1016/j.apenergy.2018.07.046).
- [4] R. Loonen, M. Trčka, D. Cóstola, J.L.M. Hensen, Climate adaptive building shells: State-of-the-art and future challenges, *Renewable and Sustainable Energy Reviews*. (n.d.) 483–493. doi:[10.1016/j.rser.2013.04.016](https://doi.org/10.1016/j.rser.2013.04.016).
- [5] M. Addington, *Smart materials and technologies in architecture*, 2002.
- [6] M. Konstantoglou, A. Tsangrassoulis, Dynamic operation of daylighting and shading systems: a literature review, *Renewable and Sustainable Energy Reviews*. (2016) 268–283. doi:[10.1016/j.rser.2015.12.246](https://doi.org/10.1016/j.rser.2015.12.246).
- [7] Y. Luo, L. Zhang, M. Bozlar, Z. Liu, H. Guo, F. Meggers, Active building envelope systems toward renewable and sustainable energy, *Renewable and Sustainable Energy Reviews*. 104 (2019) 470–491. doi:[10.1016/j.rser.2019.01.005](https://doi.org/10.1016/j.rser.2019.01.005)
- [8] C. Vailati, E. Bachtar, P. Hass, I. Burgert, M. Rüggeberg. An autonomous shading system based on coupled wood bilayer elements, *Energy and Buildings*. 158 (2018) 1013–1022. doi: [10.1016/j.enbuild.2017.10.042](https://doi.org/10.1016/j.enbuild.2017.10.042)
- [9] A. Menges, S. Reichert. Material capacity: embedded responsiveness. *Architectural Design*. 82 (2012) 52–59. doi: [10.1002/ad.1379](https://doi.org/10.1002/ad.1379)
- [10] Z. Luoa, H. Zhanga, X. Gaoa, T. Xub, Y. Fanga, Z. Zhang. Fabrication and characterization of form-stable capric-palmitic-stearic acid ternary eutectic mixture/nano-SiO₂ composite phase change material. *Energy and Buildings*. 147 (2017) 41–46. doi: [10.1016/j.enbuild.2017.04.005](https://doi.org/10.1016/j.enbuild.2017.04.005)
- [11] G. Guldentops, G. Ardito, M. Tao, S. Granados-Focil, S. Van Dessel. A numerical study of adaptive building enclosure systems using solid–solid phase change materials with variable transparency, *Energy & Buildings* 167 (2018) 240–252. doi: [10.1016/j.enbuild.2018.02.054](https://doi.org/10.1016/j.enbuild.2018.02.054)
- [12] X. Li, C. Liu, S. Feng, N. X. Fang. Broadband light management with thermochromic hydrogel microparticles for smart windows, *Joule* 3 (2019) 290–302. doi: [10.1016/j.joule.2018.10.019](https://doi.org/10.1016/j.joule.2018.10.019)
- [13] M. Formentini, S. Lenci. An innovative building envelope (kinetic façade) with Shape Memory Alloys used as actuators and sensors, *Automation in Construction*. 85 (2018) 220–231. doi: [10.1016/j.autcon.2017.10.006](https://doi.org/10.1016/j.autcon.2017.10.006)
- [14] M. Behl, K. Kratz, U. Nochel, T. Sauter, A. Lendlein. Temperature-memory polymer actuators. *PNAS* 110 (2013) 12555–12559. doi: [10.1073/pnas.1301895110](https://doi.org/10.1073/pnas.1301895110)
- [15] R. Baetens, B.P. Jelle, A. Gustavsen, Properties, requirements and possibilities of smart windows for dynamic daylight and solar energy control in buildings: a state-of-the-art review, *Solar Energy Materials and Solar Cells*. 94 (2010) 87–105. doi:[10.1016/j.solmat.2009.08.021](https://doi.org/10.1016/j.solmat.2009.08.021).
- [16] A. LeCuyer, *ETFE Technology and design*, Birkhäuser, Basel, 2008.
- [17] S.D. Rezaei, S. Shannigrahi, S. Ramakrishna, A review of conventional, advanced, and smart glazing technologies and materials for improving indoor environments, *Solar Energy Materials and Solar Cells*. 159 (2017) 26–51. doi:[10.1016/j.solmat.2016.08.026](https://doi.org/10.1016/j.solmat.2016.08.026).
- [18] J.A. Veitch, G. van de Beld, G. Brainard, J.E. Roberts, Ocular lighting effects on human physiology and behaviour, *Commission Internationale de l’Eclairage*, Austria, n.d.
- [19] J. Rostron, Sick building syndrome determinants, *Journal of Retail & Leisure Property*. 7 (2008) 323–324. doi:[10.1057/rjp.2008.20](https://doi.org/10.1057/rjp.2008.20).
- [20] H. Drahonovska, Light and lighting, in: J. Rostron (Ed.), *Sick Building Syndrome. Concepts, Issues and Practice*, 1st ed., E. & F.N. Spon, London, 1997: pp. 29–56.
- [21] M. Barozzi, J. Lienhard, A. Zanelli, C. Monticelli, The sustainability of adaptive envelopes: developments of kinetic architecture, *Procedia Engineering*. 155 (2016) 275–284. doi:[10.1016/j.proeng.2016.08.029](https://doi.org/10.1016/j.proeng.2016.08.029).
- [22] M. Casini, *Smart buildings: advanced materials and nanotechnology to improve energy-efficiency and environmental performance*, Woodhead Publishing Ltd, Amsterdam, 2016.
- [23] C.M. Lampert, Optical switching technology for glazings, *Thin Solid Films*. 236 (1993) 6–13. doi:[10.1016/0040-6090\(93\)90633-Z](https://doi.org/10.1016/0040-6090(93)90633-Z).
- [24] C.M. Lampert, Smart switchable glazing for solar energy and daylight control, *Solar Energy Materials and Solar Cells*. 52 (1998) 207–221. doi:[10.1016/S0927-0248\(97\)00279-1](https://doi.org/10.1016/S0927-0248(97)00279-1).
- [25] C.M. Lampert, Chromogenic smart materials, *Materials Today*. 7 (2004) 28–35. doi:[10.1016/S1369-7021\(04\)00123-3](https://doi.org/10.1016/S1369-7021(04)00123-3).
- [26] C.G. Granqvist, Transparent conductors as solar energy materials: a panoramic review, *Solar Energy Materials and Solar Cells*. 91 (2007) 1529–1598. doi:[10.1016/j.solmat.2007.04.031](https://doi.org/10.1016/j.solmat.2007.04.031).

- [27] C.G. Granqvist, P. Lansaker, N. Mlyuka, G. Niklasson, E. Avendano, Progress in chromogenics: new results for electrochromic and thermochromic materials and devices, *Solar Energy Materials and Solar Cells*. 93 (2009) 2032–2039. doi:[10.1016/j.solmat.2009.02.026](https://doi.org/10.1016/j.solmat.2009.02.026).
- [28] C.G. Granqvist, Chromogenic materials for transmittance control of large-area windows, *Critical Reviews in Solid State and Materials Sciences*. 16 (1990) 291–308. doi:[10.1080/10408439008242184](https://doi.org/10.1080/10408439008242184).
- [29] L. Giovannini, F. Favoino, A. Pellegrino, V. R. M. Lo Verso, V. Serra, M. Zinzi, Thermochromic glazing performance: From component experimental characterisation to whole building performance evaluation, *Applied Energy*. 251 (2019) 113335. doi:[10.1016/j.apenergy.2019.113335](https://doi.org/10.1016/j.apenergy.2019.113335)
- [30] D. Cupelli, F.P. Nicoletta, S. Manfredi, G. de Filpo, G. Chidichimo, Electrically switchable chromogenic materials for external glazing, *Solar Energy Materials and Solar Cells*. 93 (2009) 329–333. doi:[10.1016/j.solmat.2008.11.010](https://doi.org/10.1016/j.solmat.2008.11.010).
- [31] J.L. West, Polymer-dispersed liquid crystals, in: R.A. Weiss, C.K. Ober (Eds.), *Liquid-Crystalline Polymers*, American Chemical Society, Washington, DC, 1990: pp. 475–495.
- [32] P.S. Drzaic, Polymer-dispersed nematic liquid crystal for large area displays and light valves, *Journal of Applied Physics*. 60 (1986) 2142–2148. doi:[10.1063/1.337167](https://doi.org/10.1063/1.337167).
- [33] P. van Konynenberg, S. Marsland, J. McCoy, Solar radiation control using NCAP liquid crystal technology, *Solar Energy Materials*. 19 (1989) 27–41. doi:[10.1016/0165-1633\(89\)90021-X](https://doi.org/10.1016/0165-1633(89)90021-X).
- [34] D. Cupelli, F.P. Nicoletta, S. Manfredi, M. Vivacqua, P. Formoso, G. de Filpo, G. Chidichimo, Self-adjusting smart windows based on polymer-dispersed liquid crystals, *Solar Energy Materials and Solar Cells*. 93 (2009) 2008–2012. doi:[10.1016/j.solmat.2009.08.002](https://doi.org/10.1016/j.solmat.2009.08.002).
- [35] R. Vergaz, J.-M. Sanchez-Pena, D. Barrios, C. Vasquez, P. Contreras-Lallana, Modelling and electro-optical testing of suspended particle devices, *Solar Energy Materials and Solar Cells*. 92 (2008) 1483–1487. doi:[10.1016/j.solmat.2008.06.018](https://doi.org/10.1016/j.solmat.2008.06.018).
- [36] R. Vergaz, J.M.S. Pena, D. Barrios, I. Perez, J.C. Torres, Electrooptical behaviour and control of a suspended particle device, *Opto-Electronics Review*. 15 (2007) 154–158. doi:[10.2478/s11772-007-0013-9](https://doi.org/10.2478/s11772-007-0013-9).
- [37] J.E. Fernández, Materials for aesthetic, energy-efficient, and self-diagnostic buildings, *Science*. 315 (2007) 1807–1810. doi:[10.1126/science.1137542](https://doi.org/10.1126/science.1137542).
- [38] C.G. Granqvist, Electrochromics for smart windows: oxide-based thin films and devices, *Thin Solid Films*. 564 (2014) 1–38. doi:[10.1016/j.tsf.2014.02.002](https://doi.org/10.1016/j.tsf.2014.02.002).
- [39] View. Dynamic Insulating Glass Unit (IGU). Data Sheet, (n.d.). <https://view.com/assets/pdfs/igu-data-sheet-us.pdf> (accessed August 8, 2019).
- [40] SageGlass performance and acoustical data, (n.d.). https://www.sageglass.com/sites/default/files/mkt-043_performance_and_acoustical_data_flyer.pdf (accessed August 8, 2019).
- [41] D. Barrios, R. Vergaz, J.M. Sanchez-Pena, C.G. Granqvist, G.A. Niklasson, Toward a quantitative model for suspended particle devices: optical scattering and absorption coefficients, *Solar Energy Materials and Solar Cells*. 111 (2013) 115–122. doi:[10.1016/j.solmat.2012.12.012](https://doi.org/10.1016/j.solmat.2012.12.012).
- [42] J. Lienhard, S. Schleicher, S. Poppinga, T. Masselter, M. Milwich, T. Speck, J. Knippers, Flectofin: a hingeless flapping mechanism inspired by nature, *Bioinspiration and Biomimetics*. 6 (2011) 045001. doi:[10.1088/1748-3182/6/4/045001](https://doi.org/10.1088/1748-3182/6/4/045001)
- [43] A. Karanouh, E. Kerber, Innovations in dynamic architecture, *Journal of Facade Design and Engineering* 3 (2015) 185–221. doi:[10.3233/FDE-150040](https://doi.org/10.3233/FDE-150040)
- [44] Z. Drozdowski, S. Gupta, Adaptive fritting as case exploration for adaptivity in architecture, *ACADIA 09: reForm()* (2009) 105–109. http://cumincad.scix.net/data/works/att/acadia09_105.content.pdf
- [45] F. Alotaibi, The role of kinetic envelopes to improve energy performance in buildings, *Journal of Architectural Engineering Technology*. 4 (2015) 1000149. doi:[10.4172/2168-9717.1000149](https://doi.org/10.4172/2168-9717.1000149)
- [46] Z. Drozdowski, S. Gupta, Adaptive fritting as case exploration for adaptivity in architecture, in: *ACADIA 09: ReForm(): Building a Better Tomorrow: Proceedings of the 29th Annual Conference of the Association of Computer Aided Design in Architecture*, 2009.
- [47] B. Kolarevic, V. Parlac, Adaptive, responsive building skins, in: B. Kolarevic, V. Parlac (Eds.), *Building Dynamics: Exploring Architecture of Change*, Routledge Taylor & Francis Group, 2015: pp. 69–88.
- [48] M. Addington, D. Schodek, *Smart materials and technologies: for the architecture and design professions*, Architectural Press, Oxford, 2005.
- [49] A. Gómez-González, J. Neila, J. Monjo-Carrió, Pneumatic skins in architecture. Sustainable trends in low positive pressure inflatable systems, *Procedia Engineering*. 21 (2011) 125–132. doi:[10.1016/j.proeng.2011.11.1995](https://doi.org/10.1016/j.proeng.2011.11.1995).
- [50] G. Wypych, *Handbook of polymers*, 2nd ed., ChemTec Publishing, 2016.
- [51] J. Knippers, J. Cremers, M. Gabler, J. Lienhard, *Construction manual for polymers + membranes*, Birkhäuser, Basel, 2011.
- [52] S. Jeska, *Transparent plastics - design technology*, Birkhäuser, Basel, 2008.
- [53] J.C. Chilton, Lightweight envelopes: ethylene tetra-fluoro-ethylene foil in architecture, *Construction materials*. 166 (2013) 343–357. doi:[10.1680/coma.12.00049](https://doi.org/10.1680/coma.12.00049).
- [54] Nowofol, Nowofol clear ETFE product information, n.d. <https://www.etfe-film.com/files/etfe/pdf/Product-Information-NOWOFOLON-ET-6235-Z.pdf> (accessed May 20, 2019).
- [55] Architen Landrell, ETFE: an economical alternative to glass, (2011). <http://www.architen.com/articles/etfe-foil/> (accessed May 20, 2019).
- [56] J. Hu, W. Chen, B. Zhao, D. Yang, Buildings with ETFE foils: a review on material properties, architectural performance and structural behavior, *Construction and Building Materials*. 131 (2017) 411–422. doi:[10.1016/j.conbuildmat.2016.11.062](https://doi.org/10.1016/j.conbuildmat.2016.11.062).
- [57] Birdair, ETFE film structures, 2015. http://www.birdair.com/system/files/Birdair_ETFE_6pg_WEB.pdf (accessed May 20, 2019).
- [58] B. Martin, D. Masih, B. Lau, P. Beccarelli, J. Chilton, An evaluation of thermal and lighting performance within an ETFE structure, in: C. Gorse, M. Dastbaz (Eds.), *International SEEDS Conference*, Leeds Beckett University UK, 2015: pp. 47–58.
- [59] H. Liu, B. Li, Z. Chen, T. Zhou, Q. Zhang, Solar radiation properties of common membrane roofs, *Materials and Design*. 105 (2016) 268–277. doi:[10.1016/j.matdes.2016.05.068](https://doi.org/10.1016/j.matdes.2016.05.068).
- [60] Nowofol, NOWOFOLON ET 6235 Z-IR, n.d. <https://www.etfe-film.com/files/etfe/pdf/Product-Information-NOWOFOLON-ET-6235-Z-IR.pdf> (accessed May 20, 2019).
- [61] J. Cremers, H. Marx, Comparative study of a new IR-absorbing film to improve solar shading and thermal comfort for ETFE structures, *Procedia Engineering*. 155 (2016) 113–120. doi:[10.1016/j.proeng.2016.08.012](https://doi.org/10.1016/j.proeng.2016.08.012).

- [62] J. Cremers, H. Marx, 3D-ETFE: development and evaluation of a new printed and spatially transformed foil improving shading, slight quality, thermal comfort and energy demand for membrane cushion structures, *Energy Procedia*. 122 (2017) 115–120. doi:[10.1016/j.egypro.2017.07.306](https://doi.org/10.1016/j.egypro.2017.07.306).
- [63] H. Poirazis, M. Kragh, C. Hogg, Energy modeling of ETFE membranes in building applications, in: Glasgow, 2009: pp. 696–703. https://pdfs.semanticscholar.org/9748/99f7e36a84e5a46d1deb3193178bc068f1a6.pdf?_ga=2.209390546.1107520845.1557329803-451098429.1557329803 (accessed May 20, 2019).
- [64] J.E. Mark, ed., *Polymer data handbook*, 2nd ed., Oxford University Press, New York, 2009.
- [65] T. Fujii, PDMS-based microfluidic devices for biomedical applications, *Microelectronic Engineering*. 907 (2002) 61–62. doi:[10.1016/S0167-9317\(02\)00494-X](https://doi.org/10.1016/S0167-9317(02)00494-X).
- [66] D.C. Duffy, J. Cooper McDonald, O.J.A. Schueller, G.M. Whitesides, Rapid prototyping of microfluidic systems in poly(dimethylsiloxane), *Analytical Chemistry*. 70 (1998) 4974–4984. doi:[10.1021/ac980656z](https://doi.org/10.1021/ac980656z).
- [67] J. Cooper McDonald, D.C. Duffy, J.R. Anderson, D.T. Chiu, H. Wu, O.J.A. Schueller, G.M. Whitesides, Fabrication of microfluidic systems in poly(dimethylsiloxane), *Electrophoresis*. 21 (2000) 27–40. doi:[10.1002/\(SICI\)1522-2683\(20000101\)21:1<27::AID-ELPS27>3.0.CO;2-C](https://doi.org/10.1002/(SICI)1522-2683(20000101)21:1<27::AID-ELPS27>3.0.CO;2-C).
- [68] F. Ilijevski, A.D. Mazzeo, R.F. Shepherd, X. Chen, G.M. Whitesides, Soft robotics for chemists, *Angewandte Chemie International Edition*. 50 (2011) 1890–1895. doi:[10.1002/anie.201006464](https://doi.org/10.1002/anie.201006464).
- [69] J. Lee, S. Kim, J. Lee, D. Yang, B.C. Park, S. Ryu, I. Park, A stretchable strain sensor based on a metal nanoparticle thin film for human motion detection, *Nanoscale*. 6 (2014) 11932. doi:[10.1039/c4nr03295k](https://doi.org/10.1039/c4nr03295k).
- [70] C.F. Guo, Q. Liu, G. Wang, Y. Wang, Z. Shi, Z. Suo, C.-W. Chu, Z. Ren, Fatigue-free, superstretchable, transparent, and biocompatible metal electrodes, *Proceedings of the National Academy of Sciences*. 112 (2015) 12332–12337. doi:[10.1073/pnas.1516873112](https://doi.org/10.1073/pnas.1516873112).
- [71] D.-H. Kim, N. Lu, R. Ma, Y.-S. Kim, R.-H. Kim, S. Wang, J. Wu, S.M. Won, H. Tao, A. Islam, K.J. Yu, T. Kim, R. Chowdhury, M. Ying, L. Xu, M. Li, H.-J. Chung, H. Keum, M. McCormick, P. Liu, Y.-W. Zhang, F.G. Omenetto, Y. Huang, T. Coleman, J.A. Rogers, Epidermal electronics, *Science*. 333 (2011) 838–843. doi:[10.1126/science.1206157](https://doi.org/10.1126/science.1206157).
- [72] Datasheet Bisco HT-6240 transparent solid silicone, (n.d.). <https://www.rogerscorp.com/documents/491/ems/bisco/HT-624040-Durometer-Performance-Solid-Silicone.pdf> (accessed August 19, 2019).
- [73] A.B. Ucar, O.D. Velev, Microfluidic elastomer composites with switchable vis-IR transmittance, *Soft Matter*. 8 (2012) 11232–11235. doi:[10.1039/C2SM26635K](https://doi.org/10.1039/C2SM26635K).
- [74] D. Park, P. Kim, J. Alvarenga, K. Jin, J. Aizenberg, M. Bechthold, Dynamic daylight control system implementing thin cast arrays of polydimethylsiloxane-based millimeter-scale transparent louvers, *Building and environment*. 82 (2014) 87–96. doi:[10.1016/j.buildenv.2014.07.016](https://doi.org/10.1016/j.buildenv.2014.07.016).
- [75] H.N. Apostoleris, M. Chiesa, M. Stefancich, Improved transparency switching in paraffin-PDMS composites, *Journal of Materials Chemistry C*. 3 (2015). doi:[10.1039/C4TC02546F](https://doi.org/10.1039/C4TC02546F).
- [76] A.C.C. Rotzetter, R. Fuhrer, R.N. Grass, C.M. Schumacher, P.R. Stoessel, W.J. Stark, Micro mirror polymer composite offers mechanically switchable light transmittance, *Advanced Engineering Materials*. 16 (2014) 878–883. doi:[10.1002/adem.201300478](https://doi.org/10.1002/adem.201300478).
- [77] F. López Jiménez, S. Kumar, P. Miguel Reis, Soft color composites with tunable optical transmittance, *Advanced Optical Materials*. 4 (n.d.) 620–626. doi:[10.1002/adom.201500617](https://doi.org/10.1002/adom.201500617).
- [78] R. Brunner, B. Keil, C. Morhard, D. Lehr, U. Wallrabe, J. Spatz, Antireflective “moth-eye” structures on tunable optical silicone membranes, *Applied Optics*. 51 (2012) 4370–4376. doi:[10.1364/AO.51.004370](https://doi.org/10.1364/AO.51.004370).
- [79] P. Kim, Y. Hu, J. Alvarenga, M. Kolle, Z. Suo, J. Aizenberg, Rational design of mechano-responsive optical materials by fine tuning the evolution of strain-dependent wrinkling patterns, *Advanced Optical Materials*. 1 (2013) 381–388. doi:[10.1002/adom.201300034](https://doi.org/10.1002/adom.201300034).
- [80] E. Lee, M. Zhang, Y. Cho, Y. Cui, J. van der Spiegel, N. Engheta, S. Yang, Tilted pillars on wrinkled elastomers as a reversibly tunable optical window, *Advanced Materials*. 26 (2014) 4127–4133. doi:[10.1002/adma.201400711](https://doi.org/10.1002/adma.201400711).
- [81] H. Hillborg, J.F. Anker, U.W. Gedde, G.D. Smith, H.K. Yasuda, K. Wilström, Crosslinked polydimethylsiloxane exposed to oxygen plasma studied by neutron reflectometry and other surface specific techniques, *Polymer*. 41 (2000) 6851–6862. doi:[10.1016/S0032-3861\(00\)00039-2](https://doi.org/10.1016/S0032-3861(00)00039-2).
- [82] S. Yang, K. Krishnacharya, P.-C. Lin, Harnessing surface wrinkle patterns in soft matter, *Advanced Functional Materials*. 20 (2010) 2550–2564. doi:[10.1002/adfm.201000034](https://doi.org/10.1002/adfm.201000034).
- [83] P.-C. Lin, S. Vajpayee, A. Jagota, C.-Y. Hui, S. Yang, Mechanically tunable dry adhesive from wrinkled elastomers, *Soft Matter*. 4 (2008) 1830–1835. doi:[10.1039/B802848F](https://doi.org/10.1039/B802848F).
- [84] P.J. Yoo, K.Y. Suh, H. Kang, H.H. Lee, Polymer elasticity-driven wrinkling and coarsening in high temperature buckling of metal-capped polymer thin films, *Physical Review Letters*. 93 (2004) 034301. doi:[10.1103/PhysRevLett.93.034301](https://doi.org/10.1103/PhysRevLett.93.034301).
- [85] H.X. Mei, R. Huang, J.Y. Chung, C.M. Stafford, H.H. Yu, Buckling modes of elastic thin films on elastic substrates, *Applied Physics Letters*. 90 (2007) 151902. doi:[10.1063/1.2720759](https://doi.org/10.1063/1.2720759).
- [86] E.P. Chan, A.J. Crosby, Spontaneous formation of stable aligned wrinkling patterns, *Soft Matter*. 2 (2006) 324–328. doi:[10.1039/B515628A](https://doi.org/10.1039/B515628A).
- [87] J.Y. Chung, A.J. Nolte, C.M. Stafford, Diffusion-controlled, self-organized growth of symmetric wrinkling patterns, *Advanced Materials*. 21 (2009) 1358–1362. doi:[10.1002/adma.200803209](https://doi.org/10.1002/adma.200803209).
- [88] M. Guvendiren, S. Yang, J.A. Burdick, Swelling-induced surface patterns in hydrogels with gradient crosslinking density, *Advanced Functional Materials*. 19 (2009) 3038–3045. doi:[10.1002/adfm.200900622](https://doi.org/10.1002/adfm.200900622).
- [89] J.Y. Chung, A.J. Nolte, C.M. Stafford, Surface wrinkling: a versatile platform for measuring thin-film properties, *Advanced Materials*. 23 (2011) 349–368. doi:[10.1002/adma.201001759](https://doi.org/10.1002/adma.201001759).
- [90] A. Schweikart, A. Fery, Controlled wrinkling as a novel method for the fabrication of patterned surfaces, *Microchim Acta*. 165 (2009) 249–263. doi:[10.1007/s00604-009-0153-3](https://doi.org/10.1007/s00604-009-0153-3).
- [91] R. Huang, Z. Suo, Wrinkling of a compressed elastic film on a viscous layer, *Journal of Applied Physics*. 91 (2002) 1135. doi:[10.1063/1.1427407](https://doi.org/10.1063/1.1427407).
- [92] H. Jiang, D.-Y. Khang, J. Song, Y. Sun, Y. Huang, J.A. Rogers, Finite deformation mechanics in buckled thin films on compliant supports, *Proceedings of the National Academy of Sciences*. 104 (2007) 15607–15612. doi:[10.1073/pnas.0702927104](https://doi.org/10.1073/pnas.0702927104).
- [93] W.T.S. Huck, N. Bowden, P. Onck, T. Pardoën, J.W. Hutchinson, G.M. Whitesides, Ordering of spontaneously formed buckles on planar surfaces, *Langmuir*. 16 (2000) 3497–3501. doi:[10.1021/la991302l](https://doi.org/10.1021/la991302l).

- [94] T. Ohzono, M. Shimomura, Ordering of microwrinkle patterns by compressive strain, *Physical Review B*. 69 (2004) 132202. doi:[10.1103/PhysRevB.69.132202](https://doi.org/10.1103/PhysRevB.69.132202).
- [95] J.Y. Chung, J.-H. Lee, K.L. Beers, C.M. Stafford, Stiffness, strength, and ductility of nanoscale thin films and membranes: a combined wrinkling - cracking methodology, *Nano Letters*. 11 (2011) 3361–3365. doi:[10.1021/nl201764b](https://doi.org/10.1021/nl201764b).
- [96] M.D. Thouless, Z. Li, N.J. Douville, S. Takayama, Periodic cracking of films supported on compliant substrates, *Journal of the Mechanics and Physics of Solids*. 59 (2011) 1927–1937. doi:[10.1016/j.jmps.2011.04.009](https://doi.org/10.1016/j.jmps.2011.04.009).
- [97] S.P. Lacour, S. Wagner, Z. Huang, Z. Suo, Stretchable gold conductors on elastomeric substrates, *Applied Physics Letters*. 82 (2003) 2404. doi:[10.1063/1.1565683](https://doi.org/10.1063/1.1565683).
- [98] S.P. Lacour, D. Chan, S. Wagner, T. Li, Z. Suo, Mechanisms of reversible stretchability of thin metal films on elastomeric substrates, *Applied Physics Letters*. 88 (2006) 204103. doi:[10.1063/1.2201874](https://doi.org/10.1063/1.2201874).
- [99] K. Hinz, J. Alvarenga, P. Kim, D. Park, J. Aizenberg, M. Bechthold, Pneumatically adaptive light modulation system (PALMS) for buildings, *Materials and Design*. 152 (2018) 156–167. doi:[10.1016/j.matdes.2018.04.044](https://doi.org/10.1016/j.matdes.2018.04.044).
- [100] N. Bowden, W.T.S. Huck, K.E. Paul, G.M. Whitesides, The controlled formation of ordered, sinusoidal structures by plasma oxidation of an elastomeric polymer, *Applied Physics Letters*. 75 (1999) 2557. doi:[10.1063/1.125076](https://doi.org/10.1063/1.125076).
- [101] N. Bowden, S. Brittain, A.G. Evans, J.W. Hutchinson, G.M. Whitesides, Spontaneous formation of ordered structures in thin films of metals supported on an elastomeric polymer, *Nature*. 393 (1998) 146–149. doi:[10.1038/30193](https://doi.org/10.1038/30193).
- [102] C.G. Martin, T.T. Su, I.H. Loh, E. Balizer, S.T. Kowel, P. Kornreich, The metallization of silicone polymers in the rubbery and glassy state, *Journal of Applied Physics*. 53 (1982) 797–799. doi:[10.1063/1.329995](https://doi.org/10.1063/1.329995).
- [103] J. Genzer, J. Groenewold, Soft matter with hard skin: from skin wrinkles to templating and material characterization, *Soft Matter*. 2 (2006) 310–323. doi:[10.1039/B516741H](https://doi.org/10.1039/B516741H).
- [104] C. Harrison, C.M. Stafford, W.H. Zhang, A. Karim, Sinusoidal phase grating created by a tunably buckled surface, *Applied Physics Letters*. 85 (2004) 4016. doi:[10.1063/1.1809281](https://doi.org/10.1063/1.1809281).
- [105] D.Y. Khang, H.Q. Jiang, Y. Huang, J.A. Rogers, A stretchable form of single-crystal silicon for high-performance electronics on rubber substrates, *Science*. 311 (2006) 208–212. doi:[10.1126/science.1121401](https://doi.org/10.1126/science.1121401).
- [106] Y. Mei, S. Kiravittaya, S. Harazim, O.G. Schmidt, Principles and applications of micro and nanoscale wrinkles, *Materials Science & Engineering*. 70 (2010) 209–224. doi:[10.1016/j.mser.2010.06.009](https://doi.org/10.1016/j.mser.2010.06.009).
- [107] E.P. Chan, S. Kundu, Q. Lin, C.M. Stafford, Quantifying the stress relaxation modulus of polymer thin films via thermal wrinkling, *ACS Applied Materials & Interfaces*. 3 (2010) 331–338. doi:[10.1021/am100956q](https://doi.org/10.1021/am100956q).
- [108] C.M. Stafford, C. Harrison, K.L. Beers, A. Karim, E.J. Amis, M.R. Vanlandingham, H.C. Kim, W. Volksen, R.D. Miller, E.E. Simonyi, A buckling-based metrology for measuring the elastic moduli of polymeric thin films, *Nature Materials*. 3 (2004) 55–550. doi:[10.1038/nmat1175](https://doi.org/10.1038/nmat1175).
- [109] M. Pretzl, A. Schweikart, C. Hanske, A. Chiche, U. Zettl, A. Horn, A. Boker, A. Fery, A lithography-free pathway for chemical microstructuring of macromolecules from aqueous solution based on wrinkling, *Langmuir*. 24 (2008) 12748. doi:[10.1021/la8021694](https://doi.org/10.1021/la8021694).
- [110] Standard solar spectra, (n.d.). <https://www.pveducation.org/pvcdrom/appendices/standard-solar-spectra>. (accessed May 20, 2019)
- [111] R. McCluney, Suggested methodologies for determining the SHGC of complex fenestration systems for NFRC ratings, For the National Fenestration Rating Council, n.d. <https://pdfs.semanticscholar.org/972a/278727c61ccf0d86004dc350ad49188a1a2e.pdf> (accessed May 20, 2019).
- [112] A. Sharda, S. Kumar, Heat transfer through glazing systems with inter-pane shading devices: a review, *Energy Technology & Policy*. 1 (2014) 23–34. doi:[10.1080/23317000.2014.969451](https://doi.org/10.1080/23317000.2014.969451).
- [113] Sattler, ETFE-Foil structures – the flexible glass, (n.d.). <https://www.sattler-global.com/textile-architecture/etfe-foils-1013.jsp> (accessed May 20, 2019).
- [114] C. Kasinalis, R.C.G.M. Loonen, D. Cóstola, J.L.M. Hensen. Framework for assessing the performance potential of seasonally adaptable facades using multi-objective optimization, *Energy and Buildings*. 79 (2014) 106–113. doi:[10.1016/j.enbuild.2014.04.045](https://doi.org/10.1016/j.enbuild.2014.04.045).
- [115] R.C.G.M. Loonen, F. Favoino, J.L.M. Hensen, M. Overend. Review of current status, requirements and opportunities for building performance simulation of adaptive facades, *Journal of Building Performance Simulation*. 10 (2017) 205–223. doi:[10.1080/19401493.2016.1152303](https://doi.org/10.1080/19401493.2016.1152303).
- [116] S. Robinson-Gayle, M. Kolokotroni, A. Cripps, S. Tanno, ETFE foil cushions in roofs and atria, *Construction and Building Materials*. 15 (2001) 323–327. doi:[10.1016/S0950-0618\(01\)00013-7](https://doi.org/10.1016/S0950-0618(01)00013-7).
- [117] P. Li, Q.S. Yang, Form finding and loading analysis of ETFE cushions using interaction numerical model, *Applied Mechanics and Materials*. 438–439 (2013) 1812–1815. doi:[10.4028/www.scientific.net/AMM.438-439.1812](https://doi.org/10.4028/www.scientific.net/AMM.438-439.1812).
- [118] Taiyo Europe. ETFE. Stylish, lightweight tensile architecture, (n.d.). <https://www.taiyo-europe.com/en/materials/etfe/> (accessed October 14, 2019).
- [119] MakMax, ETFE film, (n.d.). <https://www.makmax.com.au/etfe/65> (accessed May 20, 2019).
- [120] C. Chang, P. Chen, Human response to window views and indoor plants in the workplace, *HortScience*. 40 (2005) 1354–1359. <https://journals.ashs.org/view/journals/hortsci/40/5/article-p1354.xml> (accessed May 17, 2019).
- [121] K. Korpela, J. De Bloom, M. Sianoja, T. Pasanen, U. Kinnunen, Nature at home and at work: naturally good? Links between window views, indoor plants, outdoor activities and employee well-being over one year, *Landscape and Urban Planning*. 160 (2017) 38–47. doi:[10.1016/j.landurbplan.2016.12.005](https://doi.org/10.1016/j.landurbplan.2016.12.005).
- [122] How Low-e Glass Works, (n.d.). <http://glassed.vitroglazings.com/topics/how-low-e-glass-works> (accessed September 9, 2019).
- [123] Elastomer silicone, (n.d.). http://www.substech.com/dokuwiki/doku.php?id=elastomer_silicone (accessed May 21, 2019).
- [124] M. Planes, C. Le Coz, A. Soum, S. Carlotti, V. Rejssek-Riba, S. Lewandowski, S. Remaury, S. Solé, Polydimethylsiloxane/additive systems for thermal and ultraviolet stability in geostationary environment, *Journal of Spacecraft and Rockets*. 53 (2016) 1128–1133. doi:[10.2514/1.A33484](https://doi.org/10.2514/1.A33484).
- [125] Wacker Chemie AG, Solid and liquid silicone rubber material and processing guidelines, (n.d.). https://www.wacker.com/cms/media/publications/downloads/6709_EN.pdf (accessed May 20, 2019).
- [126] A. Wilson, ETFE foil: a guide to design, (2013). <http://www.architen.com/articles/etfe-foil-a-guide-to-design/> (accessed May 20, 2019).
- [127] R. Gomez-Moriana, Building as research: MEDIA-TIC by Cloud 9, (2010). <https://criticalista.com/2010/06/01/media-tic-by-cloud-9-architecture-as-research/> (accessed May 20, 2019).
- [128] E. Ruiz-Geli, It is all about particles, in: B. Kolarevic, V. Parlac (Eds.), *Building Dynamics: Exploring Architecture of Change*, Routledge Taylor & Francis Group, 2015.

- [129] C.Park, G. Augenbroe, N. Sadegh, M. Thitisawat, T.Messadi. Real-time optimization of a double-skin façade based on lumped modeling and occupant preference, *Building and Environment* 39 (2004) 939–948. doi: [10.1016/j.buildenv.2004.01.018](https://doi.org/10.1016/j.buildenv.2004.01.018)
- [130] A. L. Cheng, H. Bier. Adaptive building-skin components as context-aware nodes in an extended cyber-physical network, 2016 IEEE 3rd World Forum on Internet of Things (WF-IoT) (2016) 257-262. doi: [10.1109/WF-IoT.2016.7845436](https://doi.org/10.1109/WF-IoT.2016.7845436).
- [131] D. Chen, H.W. Chen, Using the Köppen climate classification to quantify climate variation and change: an example for 1901-2010, *Environmental Development*. 6 (2013) 69–79. doi:[10.1016/j.envdev.2013.03.007](https://doi.org/10.1016/j.envdev.2013.03.007).
- [132] Nowofol, NOWOFLON ETFE film - selected projects worldwide, (n.d.). <https://www.etfe-film.com/key-references> (accessed May 20, 2019).
- [133] L.V. Alexander, X. Zhang, T.C. Peterson, J. Caesar, B. Gleason, A.M.G. Klein Tank, M. Haylock, D. Collins, B. Trewin, F. Rahimzadeh, A. Tagipour, K. Rupa Kumar, J. Revadekar, G. Griffiths, L. Vincent, D.B. Stephenson, J. Burn, E. Aguilar, M. Brunet, M. Taylor, M. New, P. Zhai, M. Rusticucci, J.L. Vasquez-Aguirre, Global observed changes in daily climate extremes of temperature and precipitation, *Journal of Geophysical Research*. 111 (2006). doi:[10.1029/2005JD006290](https://doi.org/10.1029/2005JD006290).
- [134] E.M. Leung, M. Colorado Escobar, G.T. Stiubianu, S.R. Jim, A.L. Vyatskikh, Z. Feng, N. Garner, P. Patel, K.L. Naughton, M. Follador, E. Karshalev, M.D. Trexler, A.A. Gorodetsky, A dynamic thermoregulatory material inspired by squid skin, *Nature Communications*. 10 (2019) 1947. doi:[10.1038/s41467-019-09589-w](https://doi.org/10.1038/s41467-019-09589-w).

Tunable infrared transmission for energy efficient pneumatic building façades

Supplementary material

Lara Tomholt^{1,2*}, Olga Geletina¹, Jack Alvarenga², Anna V. Shneidman³, James C. Weaver²,
Matheus C. Fernandes^{2,3}, Santiago A. Mota¹, Martin Bechthold¹, Joanna Aizenberg^{2,3}

¹Harvard Graduate School of Design, 48 Quincy St., Cambridge, MA 02138, USA

²Wyss Institute for Biologically Inspired Engineering at Harvard University, 3 Blackfan Circle, Boston, MA 02115, USA

³John A. Paulson School of Engineering and Applied Sciences, Harvard University, Cambridge, MA 02138 USA

* Corresponding author; ltomholt@gsd.harvard.edu

1. Optical properties of ETFE films for architectural facades

The three ETFE films evaluated in this study for the purpose of juxtaposition with gold coated PDMS film were clear ETFE (ET 6235Z, NOWOFLON, Nowofol, Siegsdorf, Germany), infrared absorbing ETFE (ET 6235Z-IR, NOWOFLON, Nowofol, Siegsdorf, Germany) and fritted ETFE (sample provided by Birdair, Amherst, NY, USA). We evaluated their optical performance on their transmission and reflection in the 200 nm to 2600 nm light spectrum (Figure S01). The transmission data for clear ETFE and infrared absorbing ETFE were obtained from the manufacturer [1,2], while the transmission values of the silver printed dot on fritted ETFE film and reflection values for all three films were measured in the UV-Vis-IR spectrophotometer following the same procedure used for the gold coated PDMS films, as explained in Supplemental Section 3.2. Infrared absorbing ETFE significantly reduces infrared transmission compared to clear ETFE while still reflecting as little light, confirming significant absorption levels. As expected, the silver pigmented frit dot shows considerable levels of reflection, but transmits both visible light and infrared light to the same extent, which may not always be desirable in a building façade.

In addition, the samples were assessed on the clarity of view through the material (Figure S02). While clear ETFE and infrared absorbing ETFE provide a clear view through the material, the technology does not allow for adaptable infrared transmission. Instead, fritted ETFE allows for some degree of adaptability and solar gain regulation but obstructs the view to the exterior.

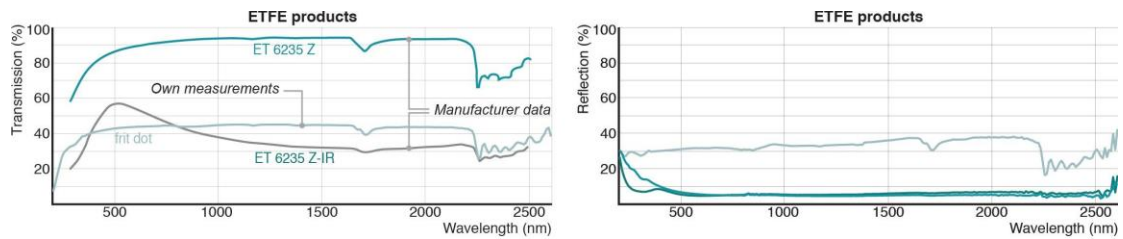


Figure S01 Visible light transmission and SHGC of treated PDMS and available ETFE and smart glazing technologies

A. Transmission and reflection properties of ETFE products, provided by the manufacturer (transmission of ET6235 Z and ET 6235 Z-IR) or measured in an identical manner as the treated PDMS samples in our study in the UV-Vis-NIR spectrophotometer (transmission frit dot and reflection of the three samples). Manufacturer data redrawn from [1] (ET 6235 Z and ET 6235 Z-IR). Clear ETFE (ET 6235 Z) is highly transmittive. As expected, a silver pigmented frit dot (Birdair) shows considerable levels of reflection. In contrast, infrared absorbing ETFE (ET 6235 Z-IR) reduces infrared transmission while reflecting little light.



Figure S02 View through ETFE films

While clear ETFE and infrared absorbing ETFE provide a clear view through the material, the technology does not allow for adaptable infrared transmission. Instead, fritted ETFE allows for some degree of adaptability and solar gain regulation but obstructs the view to the exterior.

2. Fabrication and actuation

2.1 Plasma oxidation and gold coating procedures

The PDMS films treated with oxygen plasma were exposed for 1.5 min or 3.0 min in a Femto plasma cleaner (Diener Electronic, Ebhausen, Germany) at a base pressure of 0.3 mbar and 100 Watts of power.

Gold was sputtered onto the PDMS substrates for 0.5 min, 1.0 min, 1.5 min, 2.0 min, 2.5 min or 3.0 min, using a DeskV sputter coater (Denton Vacuum, Moorestown, New Jersey, USA) at 30 mA of current. In order to determine the thickness of the gold coating partially masked glass slides underwent gold sputtering for six different durations (from 0.5 min to 3.0 min with 0.5 min intervals). Upon removal of the masking tape, atomic force microscopy with a NanoWizard 4a (JPK Instruments

AG, Berlin, Germany) was used in quantitative imaging mode to measure the surface height across the interface of uncoated and gold-coated glass (length = 90 μm) via high spatial resolution force-distance curves. For gold sputtering durations between 1.5 and 3.0 minutes the relationship between sputtering time and gold layer thickness seems relatively linear (Figure S03).

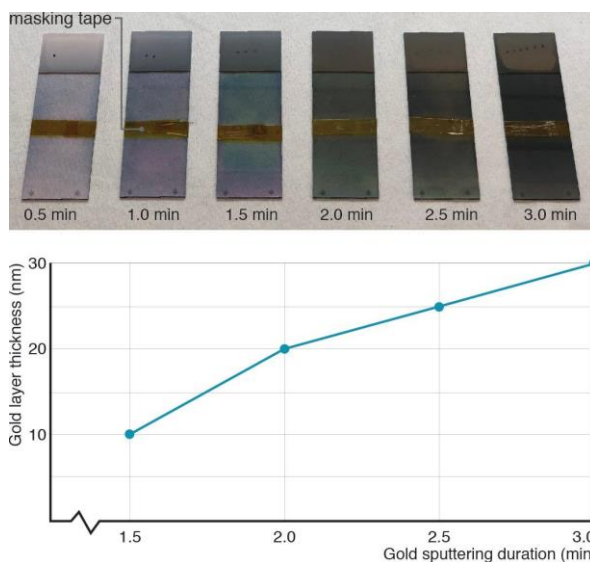


Figure S03 Gold sputtering time and resulting gold layer thickness

Atomic force microscopy (AFM) showed a relatively linear relationship between gold sputtering time and gold layer thickness for sputter times between 1.5 and 3.0 minutes. For sputter times between 2.0 and 3.0 minutes every minute of sputter time is associated with a 10 nm layer thickness.

2.2 Pneumatic actuation of PDMS film

Similar to pneumatic actuation of silicone films in other studies [3–5], an air chamber enclosed with the treated PDMS sample was pressurized allowing the PDMS to stretch. Three laser cut acrylic pieces of 1.59 mm (1/16 inch) and 6.35 mm (1/4 inch), an O-ring and screws clamp the treated PDMS film and create a disk shaped air chamber of 6.35 mm (1/4 inch) thickness for pneumatic actuation (Figure 2B). Clear ETFE (ET 6235 Z, NOWOFOLON, Nowofol, Siegsdorf, Germany [2]) was used to enclose the expansion chamber on the opposite face due to its highly infrared transmittive properties [2] and its inability to extend under low pressure. The 6.35 mm (1/4 inch) air gap between the treated PDMS sample and ETFE sheet was connected to a pneumatic source through a silicone tube with an inner diameter of 3 mm.

2.3 Finite Element (FE) analysis of pneumatically actuated PDMS film

The model presented in this study was created using the industry standard commercial FE software ABAQUS 2018 Standard/Explicit by Dassault Systemes (Johnston, Rhode Island, USA). The geometry of the model was generated using a 3D circular shell-type element to ensure computational efficiency. The shell thickness, diameter and center point translation at full actuation (250 μm , 48 mm and ~24 mm, respectively) were set to match that of the experimental set up with a refined mesh of ~94,000 shell elements.

To efficiently and accurately obtain the quasi-static solution, we performed this analysis using mass-scaling, ensuring that the model's kinetic energy is at least two orders of magnitude lower than the internal energy of the geometry. The boundary conditions for the model were set as fixed displacements ($U_1, U_2, U_3=0$) along the attachment perimeter and a uniform pressure condition was set along the lower face of the shell. The model was constructed to account for large strain deformation ('NLGEOM=ON') with the constitutive law assumed to be a linear elastic material with Young's Modulus $E = 0.87 \text{ MPa}$ and Poisson's ratio $\nu = 0.49$. It is important to note that we did not account for the visco-elastic properties of the PDMS film into our constitutive law. The FE results presented also does not account for the thin (nanometer scale) gold film. The close match between the linear elastic FE model and experimental results indicated that the viscoelasticity of the PDMS and the thin gold film would contribute only minor second order effects on the model's final results, which is supported by earlier studies [6].

In Figure 02 and Figure S04 the FE results are presented as the maximum in-plane principal logarithmic strain. This metric represents the maximum principal strain for large deformation elasticity (i.e. finite strain theory) experienced at each element of the shell. Only the in-plane strains (i.e. planar strains inducing material elongation) are considered, since, given the thin dimension of the membrane as well as the shell element assumption, out of plane strains (through the cross-section) are assumed to be uniform.

The pressure used in the model for full expansion was around 4 kPa (0.6 psi). A partitioned edge was created from the center of the circular geometry extending to its edge. The maximum in-plane logarithmic strain, coordinate, and displacement values of the 121 equally spaced nodes along the partitioned edge were exported as a data file. This was subsequently imported in the Rhinoceros and Grasshopper environment (Robert McNeel & Associates, Seattle, WA, USA), and used to track the location of four points of interest along the diameter d of the surface ($3/8d, 1/4d, 3/8d, 1/2d$) upon actuation.

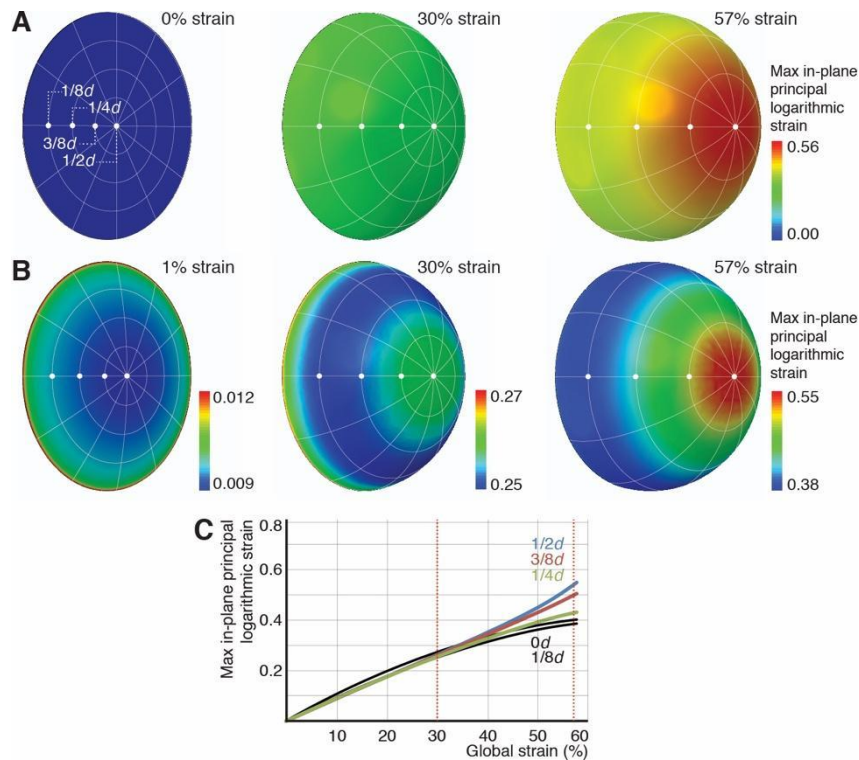


Figure S04 Localized strain in pneumatically actuated PDMS film simulated with finite element analysis

A. The simulation shows the maximum principal in-plane logarithmic strain experienced by the film upon actuation between 0% and 57% global strain. While strains are relatively similar for the points of interest ($1/8d$, $1/4d$, $3/8d$, $1/2d$) at 30% global strain, local strains start to diverge after that and show significant differences at 57% global strain. **B.** A closer look at strain differences over the surface shows varying behavior during the actuation process. At low global strains (left), local strains are higher towards the edge of the film. At high strains local strains are highest towards the center of the film (right). This causes a transition state (middle) where the low-strain center moves towards the edge of the film. **C.** The trends described in (A) and (B) are also visible when the local strains are plotted against the global strain.

3. Infrared transmission and reflection performance

3.1 Infrared

Infrared radiation (IR) is a type of electromagnetic radiation that we perceive as heat. Objects emit infrared radiation throughout the wavelength range of 700 nm to 1 mm. Solar irradiance is the amount of solar power that reaches the earth's surface per unit area and is unevenly distributed across wavelengths (Figure S05). Rays with wavelengths below 2500 nm account for 99.8% of solar spectral irradiance [7].

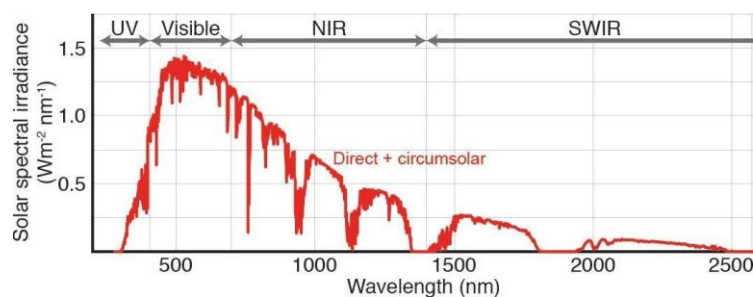


Figure S05 Variation in direct and circumsolar radiation intensities throughout the 200 - 2600 nm light spectrum

Solar irradiance is the amount of power that reaches the earth's surface per unit. The direct and circumsolar radiation intensity data show an uneven distribution between wavelengths, with increased irradiance toward the near infrared and visible light range. Chart redrawn from [7].

Due to the variation of solar intensity throughout the spectrum, the overall transmission of the material was obtained through a weighted average ("weighted average $T_{WA}\%$ ") over the 710 – 2600 nm near infrared radiation spectrum, using direct and circumsolar radiation intensities [7]. This gave us the best indication of the material's total solar heat transmission and reflection.

3.2 Sample characterization in the UV-Vis-NIR spectrophotometer

The infrared transmittance and reflectivity of the samples were characterized using a UV-Vis-NIR spectrophotometer either in conjunction with an integrating sphere, which collects all of the transmitted or reflected light within the sphere, or a variable angle detector, which provides the intensity of transmitted or reflected light for a particular collection angle. The UV-Vis-Spectrophotometer instrument used in this study (Cary 7000, Agilent Technologies, Santa Clara, CA, USA) has a detection range of wavelengths ranging from 200 to 2700 nm, and data was acquired at 10 nm intervals. The integrating sphere was used to acquire transmission (uniaxially actuated samples) and reflection (both uniaxially and pneumatically actuated samples) values. The integrating sphere allows for data acquisition of the total transmission and reflection (accounting for specular and diffuse rays), and is therefore ideally suited to capture potential diffuse scattering from the treated PDMS films [8]. Transmission data is obtained by placing the sample in front of the integrating sphere, reflection data is collected by placing the sample behind the integrating sphere.

The integrating sphere was less suitable to measure transmission values for the pneumatically actuated sample due to space limitations in the instrument. Thus, the Universal Measurement Accessory (UMA), which consists of a variable angle sample mount and detector positioning, was used to acquire transmission data for pneumatically actuated samples. The angle of the photodetector was set to capture diffusely transmitted light diverging up to 6° from the direct transmission angle.

Both in the Integrating Sphere and UMS, the sample is placed with the treated side facing the origin of the light beam. Each sample underwent one actuation cycle before measurements were obtained.

Measurements of uniaxially strained films were taken at normal incidence at the center of the sample (a single spot of a few millimeters in diameter). Taking into account the variation in localized

strains (Figure 2, Supplemental Section 2.3), measurements of pneumatic samples were taken at points across the sample diameter d ($1/4d$, $3/8d$ and $1/2d$), with the light at normal incidence to the surface.

3.3 Optical performance of uniaxial samples

Spectrophotometric analysis shows high visible light transmissions relative to the rest of the spectrum (discernable in the peak around 500 nm) in any of the treated samples and actuation strains (Figure 3A and Figure S06). This material attribute would be beneficial in a building façade, allowing relatively more visible light to be transmitted while blocking infrared to prevent solar heat gain.

Analysis revealed that the extent of pre-stretching during treatment determines the sample's critical strains to transmit the least and greatest amount of infrared radiation, namely the pre-stretched strain and the strain furthest from that, respectively (Figure 3AB and Figure S06). The weighted averages for transmission demonstrated that the highest level of tunability can be achieved by eliminating oxygen plasma exposure from the sequence of treatments (Figure 3B). This phenomenon could potentially be the result of an anti-reflective effect due to index-matching of the oxidized layer and PDMS, but further research is required to provide an explanation. A detailed examination of the full parameter space shows the relationship between gold sputtering time, actuation strain and infrared transmission (Figure S07).

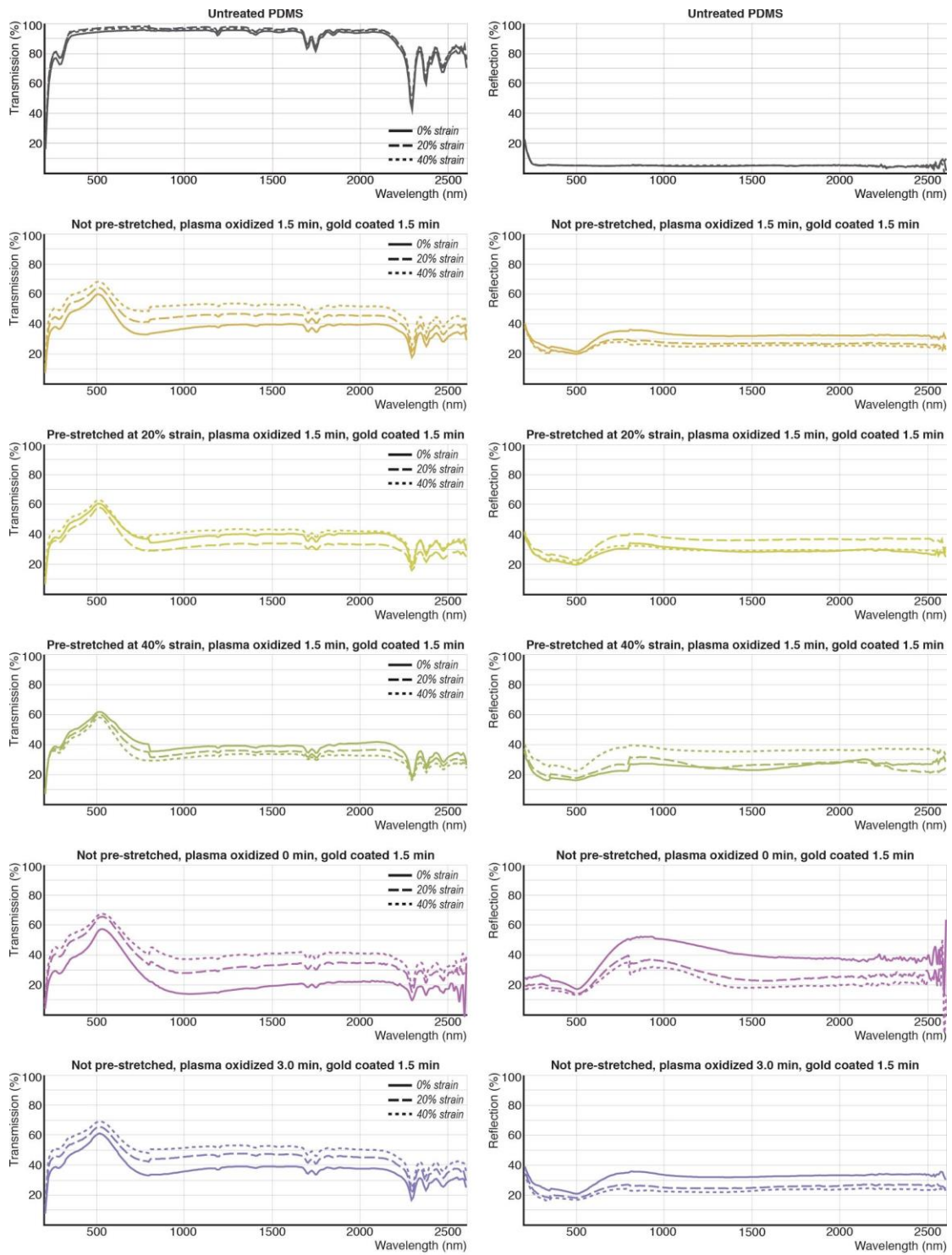


Figure S06 UV-Vis-NIR transmission and reflection

Transmission and reflection performance of (treated) PDMS samples, uniaxially strained, at wavelengths between 200 and 2600 nm at 10 nm intervals.

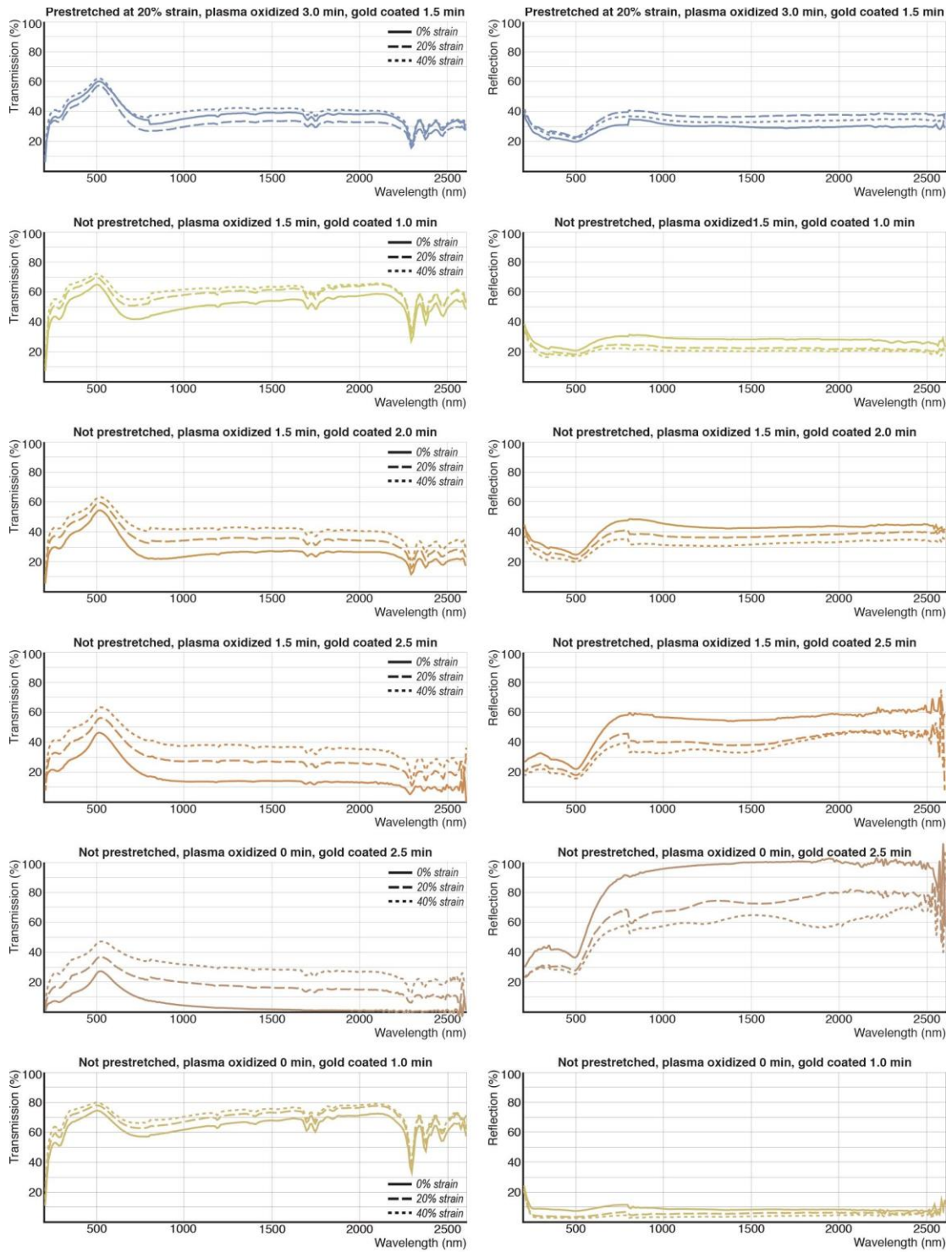


Figure S06 (continued)

UV-Vis-NIR transmission and reflection

Transmission and reflection performance of (treated) PDMS samples, uniaxially strained, at wavelengths between 200 and 2600 nm at 10 nm intervals.

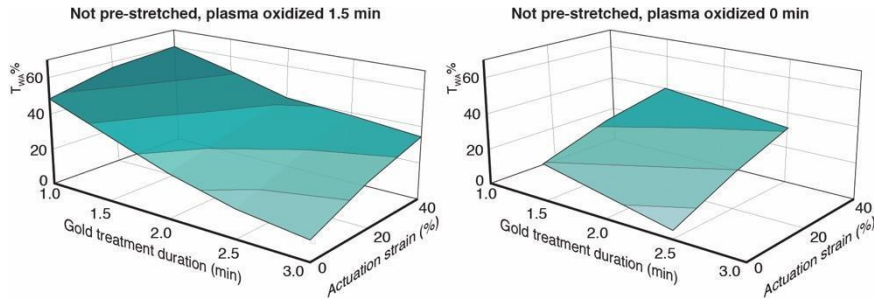


Figure S07 *Surface treatment and performance*

The plots show a full summary of experimental parameter space. The surface geometry of the 3D plots clarifies the relationship between gold treatment duration and optical performance.

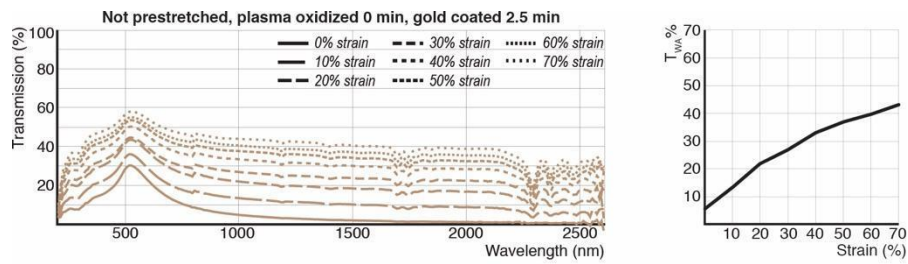


Figure S08 *Optical transmission of a sample stretched beyond 40% strain*

Uniaxially straining the material beyond 40% strain, which the material allows for, can significantly increase the materials adaptable range.

3.4 Optical performance of pneumatic sample

The transmission values at $1/8d$ were not able to be measured in the UV-Vis-NIR spectrophotometer and were estimated based on the local strains experienced. The trendline seen in Figure 3E with a formula of $y = 77.5x + 13.3$ was used to calculate those local transmission values. Subsequently, the surface area of the pneumatically actuated film was subdivided into areas around $1/8d$, $1/4d$, $3/8d$, and $1/2d$ of roughly equal size. (Figure S09C), and the formulas below used to calculate the overall surface transmission.

$$T_{full\ srf\ 0\% \ strain} = \frac{T_{1/2d\ 0\% \ strain} + T_{3/8d\ 0\% \ strain} * 8 + T_{1/4d\ 0\% \ strain} * 16 + T_{1/8d\ 0\% \ strain} * 25}{50}$$

$$T_{full\ srf\ 30\% \ strain} = \frac{T_{1/2d\ 30\% \ strain} + T_{3/8d\ 30\% \ strain} * 9 + T_{1/4d\ 30\% \ strain} * 19 + T_{1/8d\ 30\% \ strain} * 23}{52}$$

$$T_{full\ srf\ 57\% \ strain} = \frac{T_{1/2d\ 57\% \ strain} + T_{3/8d\ 57\% \ strain} * 10 + T_{1/4d\ 57\% \ strain} * 24 + T_{1/8d\ 57\% \ strain} * 28}{63}$$

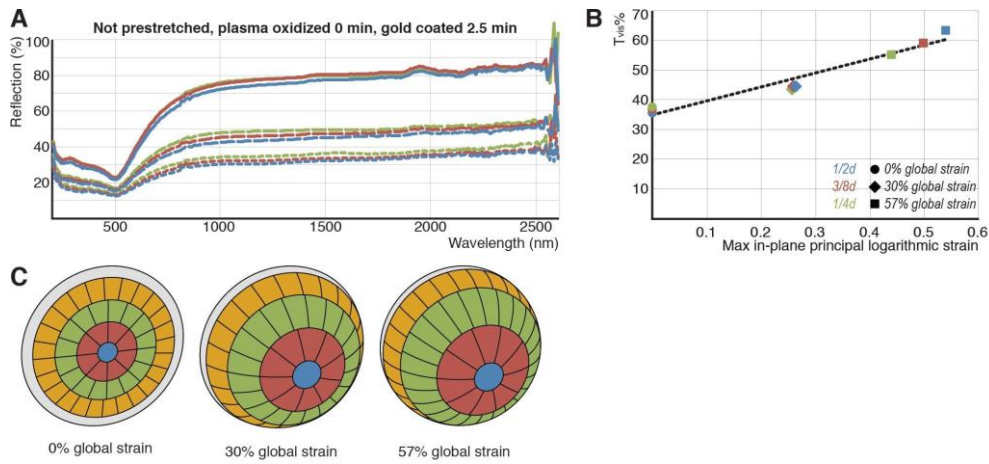


Figure S09 *Optical performance of the pneumatic sample*

A. Reflection values for pneumatically actuated film. **B.** The local strains obtained from FEA and average visible light transmissions show a clear linear correlation. **C.** To calculate the overall surface transmission, the surface area of the actuated film was subdivided into areas of equal size around $1/8d$ (yellow), $1/4d$ (green), $3/8d$ (red), $1/2d$ (blue). The area count of each respective color was used in the formulas to calculate the overall performance.

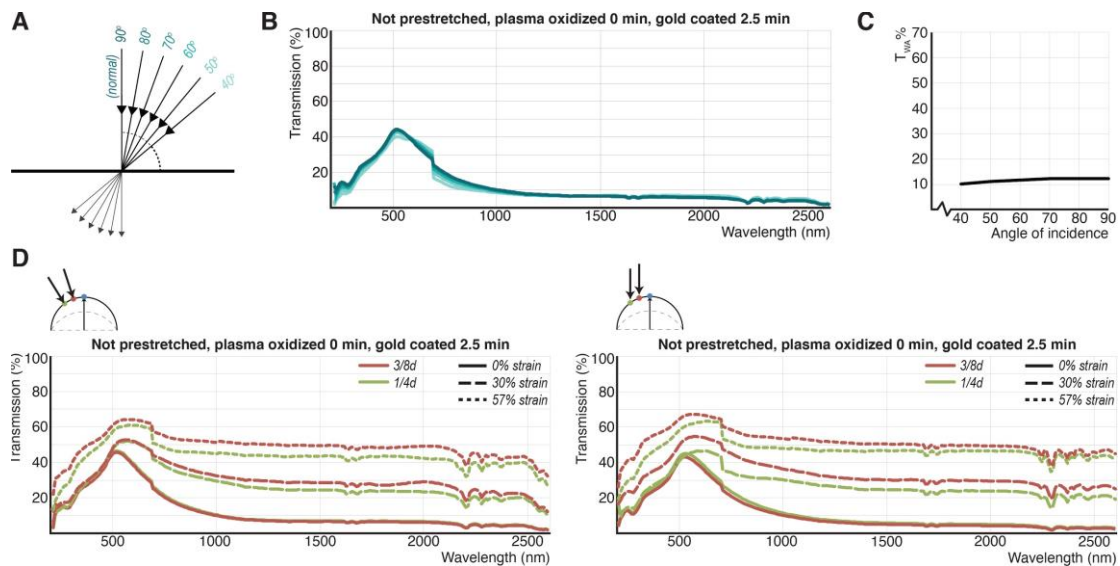


Figure S10 *Impact of angle of incidence on optical performance*

A. Angles of incidence measured at a pneumatically actuated sample at 0% global strain. **B.** Measurements show only minimal changes in transmission. Largest changes are measured around 700 nm, which can likely be attributed to machine artifacts (such as detector and filter changes). **C.** A comparison of weighted average transmission of the 710-2600 nm spectrum ($T_{WA}\%$) confirms negligible changes in near infrared transmission upon changes in the angle of incidence. **D.** The optical transmission at (left) normal incidence, and (right) normal incidence (both $1/8d$ and $1/4d$ at 0% strain), 73.2° ($3/8d$), 55.3° ($1/4d$, 30% strain), 64.8° ($3/8d$, 57% strain), and 42.2° ($1/4d$, 57% strain) show slight differences.

4. Microscale surface characteristics and infrared transmission

4.1 Uniaxially actuated samples

Each sample underwent one actuation cycle before microscope imaging. The treated PDMS films were examined at 20x magnification in an optical microscope. The films were positioned in the same orientation and observed at the approximate center of the sample.

If the actuation strain is lower than the treatment strain, wrinkles run perpendicular to the actuation axis. If the actuation strain is higher than the treatment strain, wrinkles run parallel to the actuation axis (Figure S11). For all cases, linear cracks in the rigid top surface run perpendicular to the direction of the wrinkles. These phenomena result in interesting surface morphologies when a pre-stretched sample is stretched beyond its treatment strain: wrinkles change direction parallel to the strain, and cracks perpendicular to the direction of stretch appear in addition to those running parallel. The wrinkles disappear when the applied strain matches the strain the sample was treated in. These observations agree well with wrinkling and cracking trends demonstrated in preceding studies [5,9,10].

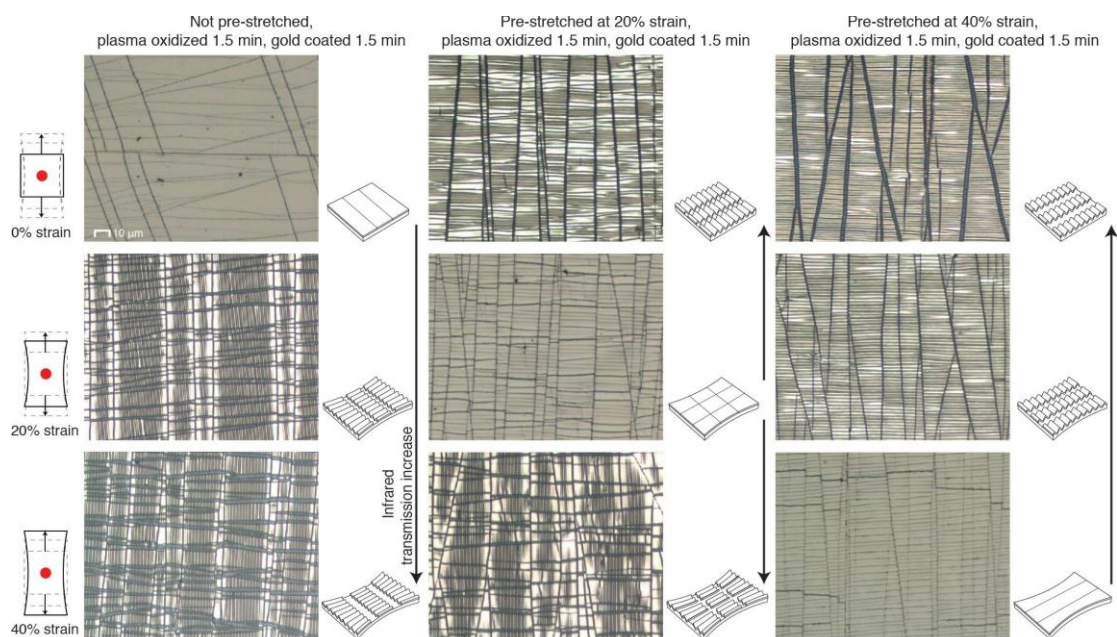


Figure S11 Surface characterization with optical microscopy of samples with various pre-stretching rates during treatment

The samples display no wrinkles and smaller cracks in the strains at which the PDMS film was stretched during treatment. Upon actuation to 20% and 40% strain, the not pre-stretched sample shows cracks perpendicular to the actuation axis that increase in width as the actuation strain increases. The direction of cracks is parallel to the actuation axis in the sample pre-stretched at 40% strain. The sample pre-stretched at 20% strain shows cracks parallel to the actuation axis at strains lower than 20% and a grid of cracks running both parallel and perpendicular to the actuation axis at strains higher than 20%. In these three samples, the increase in crack width upon either relaxation or actuation of the material corresponds with an increase in infrared transmission as measured with the spectrophotometer (Section 4).

Uniaxially actuated samples treated for the same duration with oxygen plasma and gold - yet at different strains - vary in optical transmission per actuation strain, which can be attributed to the extent of crack surface area (Figure S12A). In addition, the analysis reveals that the greater adaptability of infrared transmission for samples with a longer gold sputtering time, as observed earlier, can be attributed to a greater difference in surface crack area (Figure S12B), which, in turn, is likely caused by the increased thickness of the stiff gold layer. Although analysis has shown crack surface area correlates with infrared transmission, additional analysis is needed to understand the role plasma oxidation plays in generating cracking structures of a certain size and how crack width might contribute to overall transmission levels.

Surface analyses on microscope images at 20x magnification, with a capture area of 84000 μm^2 were performed in Adobe Photoshop, by manually selecting the areas exposed by cracks, obtaining the pixel count within those selections and subsequently calculating the percentage of the full image pixel count.

Analysis with intermittent contact (AC) mode atomic force microscopy (NanoWizard 4a, JPK Instruments AG, Berlin, Germany) using a pyramidal-tipped cantilever (radius of curvature, $R < 10$ nm; spring constant, $k = 23$ N/m) confirmed the presence of wrinkles and their tunable amplitudes and frequency (Figure S13).

Scanning electron microscopy (SEM) analysis (Figure S14) was a valuable tool in determining the quality of the gold surface finish. A small section of roughly one cm^2 from the center of each sample was cut with a scalpel to create flat pieces that could easily be clipped onto an SEM mount for imaging. SEM images were obtained using the secondary electron detector of an FESEM Ultra 55 (Zeiss, White Plains, NY, USA) scanning electron microscope, employing an accelerating voltage of 2.5 kV, 30 μm aperture, and at a ~ 3 mm working distance. The high-resolution images confirmed a high-quality smooth gold film without major delamination from the PDMS substrate.

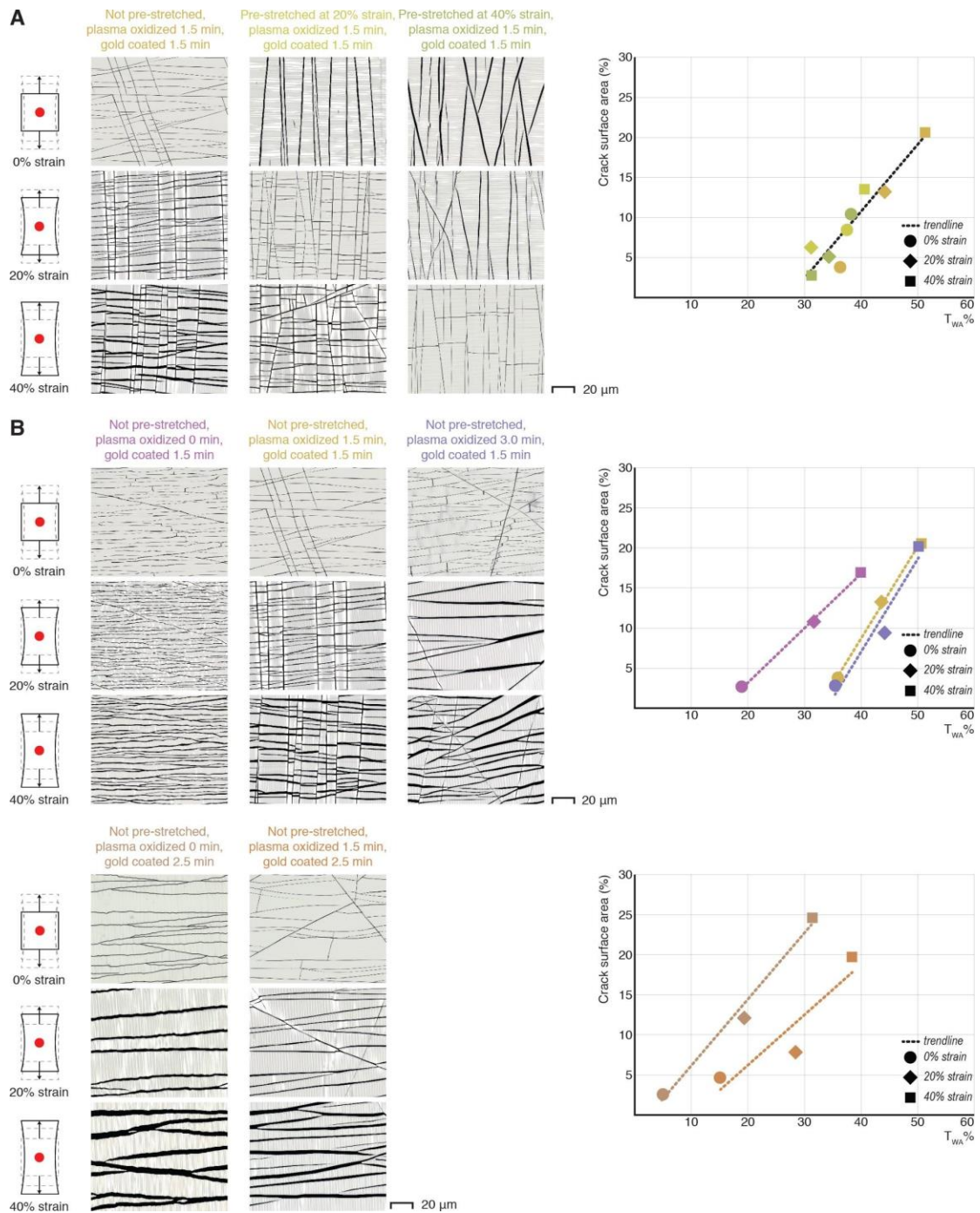


Figure S12 Surface cracking area in relation to treatment durations and infrared transmission

High contrast optical microscope images of uniaxially actuated treated PDMS films. **A.** Despite receiving treatment at different pre-stretching strains, weighted average transmission levels ($T_{wa}\%$) of the three samples seem to correlate with measured crack surface areas. **B.** The analysis of not pre-stretched samples shows that crack surface areas correlate with infrared transmission.

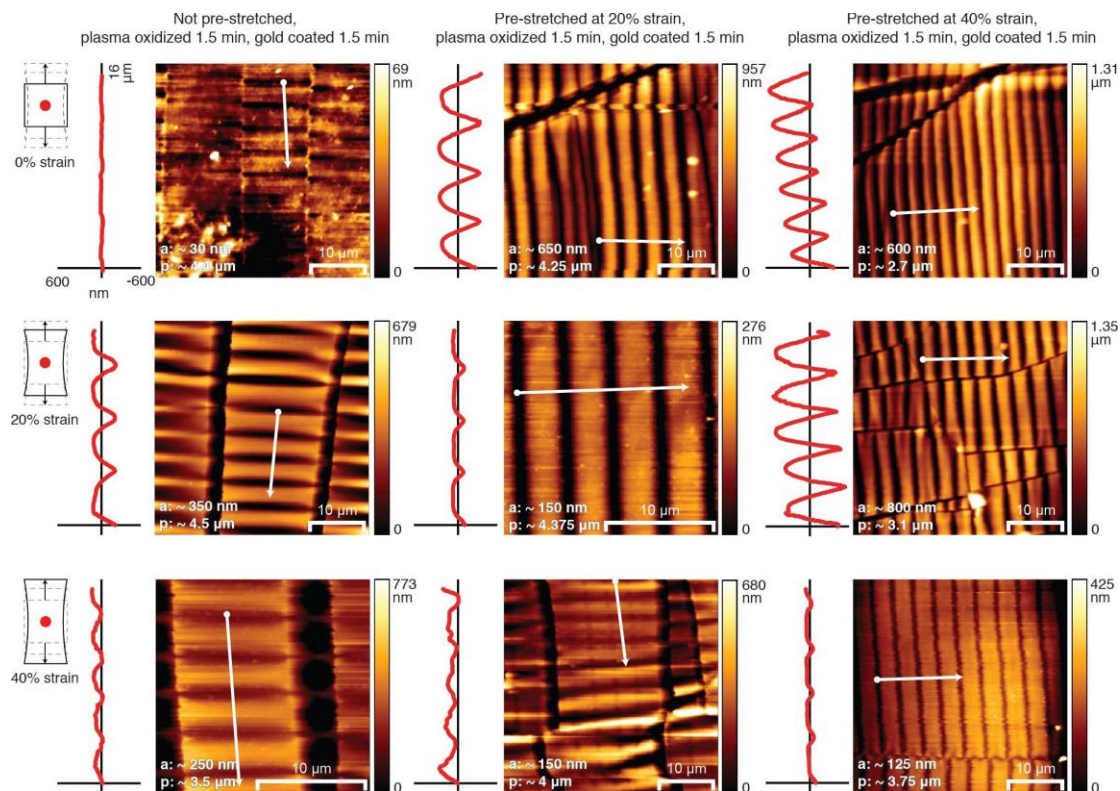


Figure S13 Atomic force microscopy (AFM) analysis of wrinkle formations as a function of pre-stretching strain and actuation strain.

The frequency (p) and amplitude (a) of wrinkles on the surface can be distinguished with the color gradient (right) indicating the relative height of the surface. A single trace running through a wave (white line) was analyzed and its cross-sectional shape plotted (red line plot).

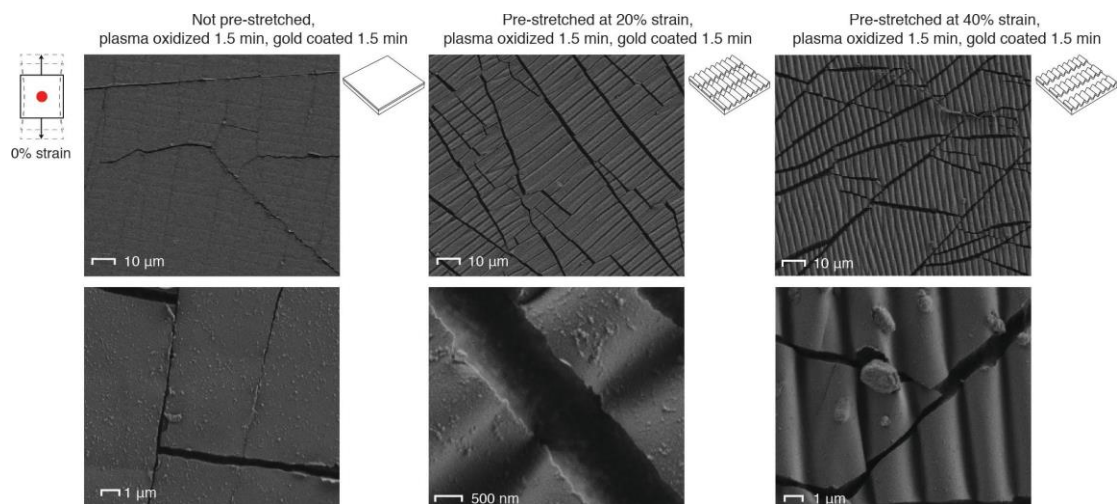


Figure S14 Scanning electron microscopy (SEM) analysis

SEM analysis confirmed a smooth gold surface coating and did not reveal significant delamination of the thin gold film. Note: these images were taken at different locations on the sample and in different orientations.

4.2 Pneumatically actuated sample

The sample underwent one actuation cycle before microscope imaging. Surface analyses on microscope images at 20x magnification were performed on a capture area of $200\ \mu\text{m}^2$ following the same procedure as used for the uniaxially actuated samples (Supplemental Section 4.1).

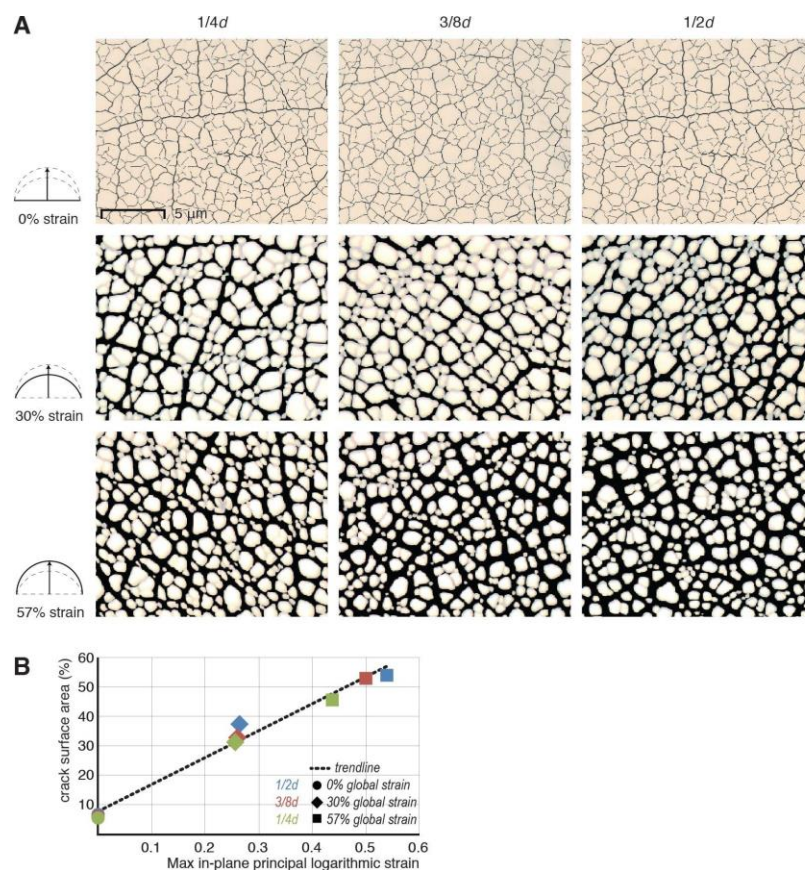


Figure S15 Crack surface area in pneumatically actuated PDMS film

A. High contrast optical microscope images of pneumatically actuated treated PDMS film (gold coated for 2.5 min without plasma oxidation and pre-stretching) show that crack widths and crack surface areas increase upon material actuation. Differences in crack surface area at 57% global strain between $1/4d$ (lowest local strain) and $1/2d$ (highest local strain) are also visible. **B.** The data shows a linear correlation between the simulated maximum in-plane logarithmic strain and measured crack surface area.

5. Heat regulation of an enclosed space

This study's spectrophotometry analysis, as described in Section 4.2, was limited to a single spot of a few millimeters in diameter at the center of the PDMS sample. However, due to the localized strain profile, the film surface displays gradients in color, translucency, and micro-scale surface morphology, suggesting potential variation in optical performance across the surface. Therefore, an experimental setup with an insulated box and heat lamp was used to verify infrared transmittive properties of the overall surface. In order to determine if spectrophotometry measurements (Section

4.2) are representative of the surface's overall performance, the tunable infrared transmittive properties were verified in an experimental setup with an insulated box and heat lamp. Additionally, these tests give an indication of the ability of the adaptable technology to regulate the interior temperature of an enclosed environment.

5.1 Experiment setup

The experiment compared the effect of untreated PDMS, clear ETFE (NOWOFLON ET 6235 Z [2]), IR-absorbing ETFE (NOWOFLON ET 6235 Z-IR [48]), and a treated PDMS sample that was gold coated for 2.5 minutes (without pre-stretching or plasma oxidation) which had proven to achieve the highest level of adaptability in infrared transmission (Section 4).

The experimental setup is shown in Figure S16ABC. The setup consisted of a 75W infrared heating lamp [11] emitting a peak spectral power around a wavelength of 800 nm, placed in front of an insulated box with sample mounted over an opening. The box is sized such that the light transmitting surface area to interior volume ratio is similar to that of a typical room in a building. The sample can be mounted on the box at different uniaxial strains (0%, 20%, and 40% strain) (Figure S16A). The exposed PDMS sample surface measures 40 by 40 mm and the interior volume of the box 473 cm³. The interior of the box is constructed out of 3.2 mm (1/8 inch) plywood with a matte white finish facing the interior space. The wooden box is insulated with foam with a thickness of 1 inch (2.54 cm) on each face of the box, to prevent accumulated heat from being released to the environment. Finally, the foam is encapsulated with aluminum tape to reflect infrared waves colliding with the exterior surface of the box, thus confining the infrared radiation contributing to heat accumulation to that which is transmitted through the "window" area. (Figure 5B) A 75W The infrared heating lamp [11] emitting a peak spectral power around a wavelength of 800 nm was placed perpendicular to the PDMS sample at a distance of 15 cm distance. A thermocouple was used to measure the air temperature at the center of the box interior (Figure S16B), and another to measure the temperature of the external environment created by the lamp directly between the heat lamp and the sample (Figure S16C). A temperature datalogger (Figure S16C) measured and recorded the two sensor values at an interval of 20 seconds. (Figure 5C)

5.2 Results

Upon switching on the lamp, the boxes reached a steady interior temperature in less than 120 minutes (Figure S17) for all samples tested. Sample performance was evaluated by the duration of the timeframe between initiation of the heat source and the interior of the box reaching the exterior temperature (t_x), as well as the temperature difference between steady state interior and exterior temperature (ΔTemp).

Supporting spectrophotometry and manufacturer data (Figure S01), untreated PDMS and clear ETFE proved to be the most optically transparent as higher interior temperatures were reached (ΔTemp of around 8 °C) and at a faster rate ($t_x \approx 10$ min) than treated PDMS film with gold (Figure S17 16). Infrared absorbing ETFE, generated lower interior temperatures than clear ETFE ($\Delta\text{Temp} \approx 4.5$ °C) (Figure S17A 16), due to its lower optical transmission (Figure S01). The measurements demonstrated

that the box incorporating the gold coated PDMS film actuated to 40% strain experienced the greatest and most rapid heat gain ($\Delta\text{Temp} \approx 3.5\text{ }^{\circ}\text{C}$ and $t_x \approx 18\text{ min}$). In contrast, the film at 0% strain increased the heat gain timeframe by around 230% ($t_x \approx 60\text{ min}$) and reduced the steady state ΔTemp to almost $0\text{ }^{\circ}\text{C}$, (Figure S17B). These results support the trends observed in spectrophotometry measurements. Depending on the actuation strain of the gold coated PDMS film, the timeframe required for the box interior to reach the exterior temperature increased up to 6 times over the untreated PDMS and ETFE films.

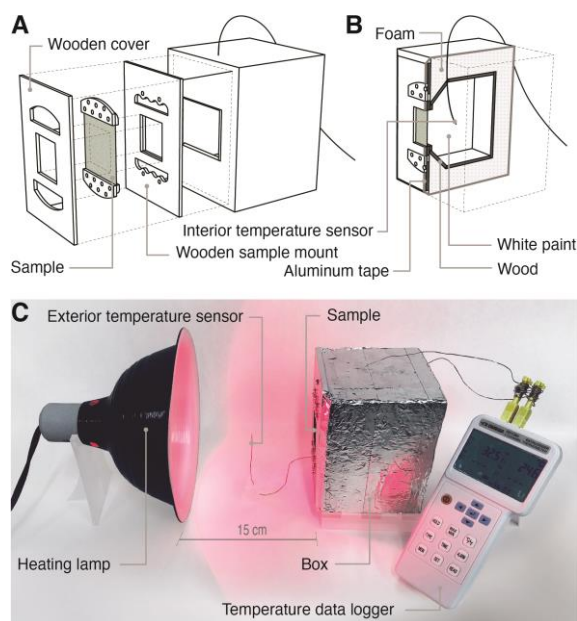


Figure S16 Experiment setup with insulated box and heat lamp

A. The PDMS samples were mounted in wooden frames at 0%, 20% or 40% strain with the treated side facing outwards, upon which the frame and cover were placed on the face of the box, sealing the box.

B. The box's plywood interior is finished with a matte white paint, insulated in foam and encapsulated with aluminum tape. The thermocouple measures the box's temperature in the center of the interior.

C. The infrared rays of the heat lamp approach the PDMS film at normal incidence. The exterior temperature sensor was placed halfway between the heat lamp and PDMS film.

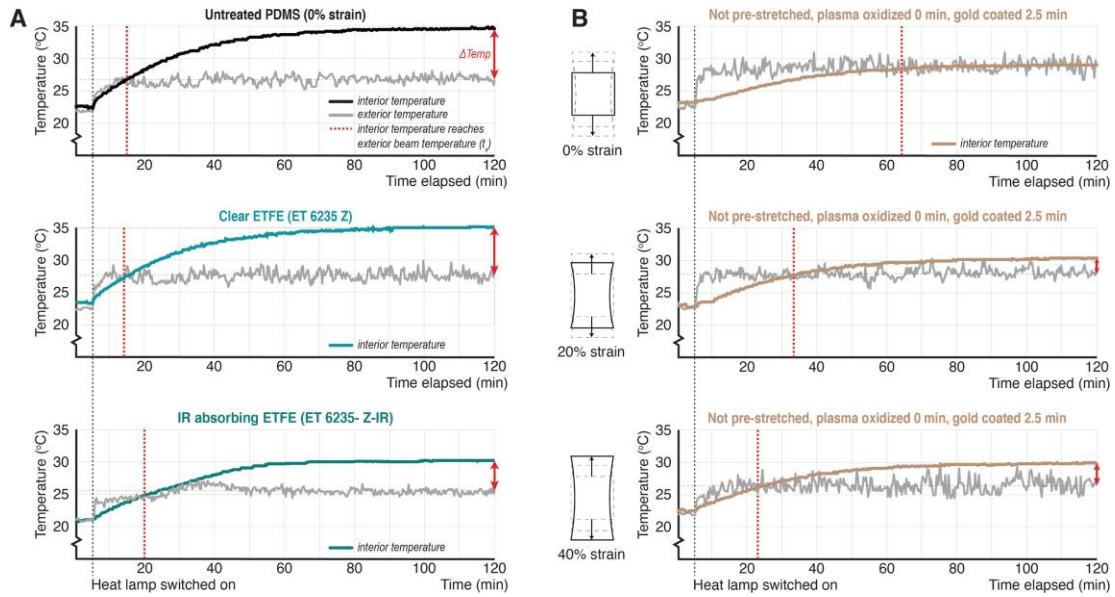


Figure S16 17 Heat regulation of an enclosed space

Sample performance is demonstrated by the duration of the timeframe between initiating the heat source (grey dashed line) and the interior of the box reaching the exterior temperature (red dashed line, t_x), and the difference between the heat lamp temperature and steady state interior temperature ($\Delta Temp$, red double arrow at $t = 120$ min). **A.** Infrared absorbing ETFE has shown to generate a lower $\Delta Temp$ (roughly 4.5 °C) than untreated PDMS and clear ETFE. The performance of the gold coated PDMS sample (Figure 5) was evaluated based on juxtaposition with these three experiments. **B.** The treated PDMS (gold coated for 2.5 minutes without pre-stretching or plasma oxidation) is least transmitting at 0% strain and most transmitting at 40% strain, confirming the trend seen with spectrophotometry analysis (Section 4).

6. Building energy savings analysis

6.1 SHGC and U-value

The SHGC is defined as the fraction of incident solar radiation that travels through the material as heat gain and has therefore a unitless value between 0 and 1. A lower SHGC means a lower solar transmission and heat gain. The U-value of a building element is a measure of conductivity thermal transmittance of non-solar heat and uses the unit W/m^2K . A lower U-value means higher insulating properties. All SHGCs and U-values calculated and presented in this paper are “center-of-glass” values.

The SHGC of a single layer material can be calculated with its transmission τ , absorption α , and inward flowing fraction N_i of the absorbed infrared with this simplified formula [12,13]:

$$SHGC = \tau + N_i * \alpha$$

Conservation of energy requires that a material’s transmittance (τ), reflection (ρ) and absorption (α) add up to 1:

$$1 = \tau + \alpha + \rho$$

This allows for inferring the film's level of absorption (α). For transmission τ and reflection ρ we used the weighted averaged values, as reported in Section 4.2. Since the inward flowing fraction N_i of radiation from absorbance was unknown, a value of 0.5 was assumed to approximate the SHGC of the treated PDMS films.

When integrated in a double layer clear ETFE cushion, the SHGC of the whole façade assembly can be obtained by multiplying the SHGC of the treated PDMS with the SHGC of a two-layer ETFE cushion ($0.925^2 = 0.86$) [2]. As such, the complete pneumatic façade system of two layers of clear ETFE and one layer of treated PDMS film will achieve a Δ SHGC of 0.29. Visible light transmission values were obtained in the same manner with a T_{VIS} of the ETFE cushion of 0.86 (0.925^2) [2].

The U-value of gold sputtered PDMS film can be calculated with the thermal conductivity (λ) and layer thickness (l) of the material's components, using the following formulas:

$$\begin{aligned} \text{Thermal resistance} & \quad R = l / \lambda \\ \text{Thermal transmittance} & \quad U = 1 / (R_{PDMS} + R_{gold}) \end{aligned}$$

Standard clear ETFE for façade application has a thickness in the range of 100-300 μm [14] and a thermal conductivity of around 0.17 W/mK, both comparable with the PDMS used in this study (250 μm and 0.15 W/mK [15]). Conforming to the formulas for thermal resistance and thermal transmittance, the thin thickness of the gold deposited layer on the PDMS film (on the order of tens of nanometers) will have a negligible impact on the film's overall U-value. For the purposes of building energy simulation, the similarity of these values led us to assume a U-value of 1.9 W/m²K for a three-layer ETFE/PDMS cushion, equal to a typical three-layer clear ETFE cushion [16].

6.2 Building energy simulation

In each simulation, one of the above mentioned façade assemblies was selected for the south façade. The simulations were run for a whole year with a one-hour time step. The simulations for the ETFE cushion with PDMS film were executed for each strain of the PDMS film (between 0% and 57% with increments of 5%) individually. Subsequently, for each hour, the strain providing the lowest energy consumption for heating and cooling was selected (favoring strains closest to 0%), and the total yearly energy consumption calculated.

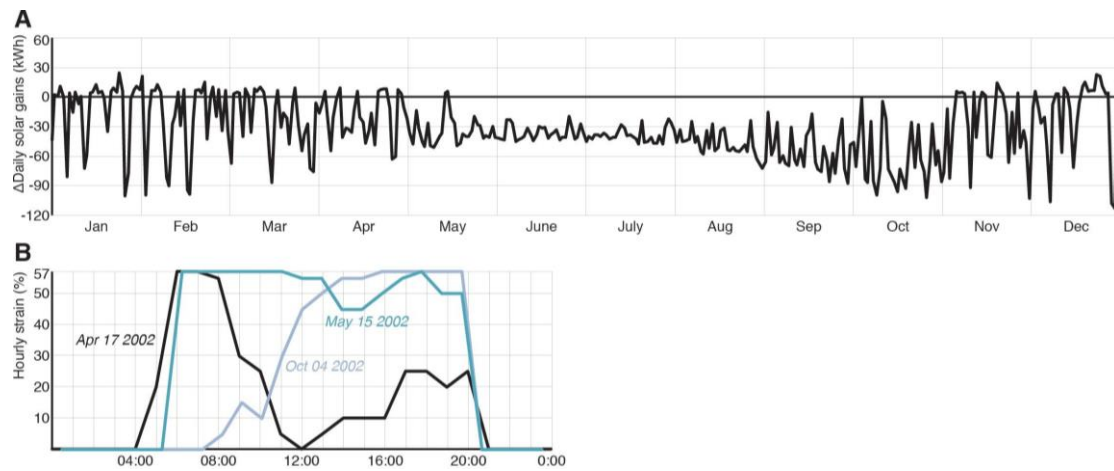
Façade	Strain (%)	SHGC	T_{VIS}	U-value (W/m ² K)
Triple-layer clear ETFE cushion ¹		0.75	0.75	1.9 ³

Triple-layer ETFE cushion with 2 layers of clear ETFE and one layer of infrared absorbing film ²		0.41	0.44	1.9
Triple-layer cushion with 2 layers of clear ETFE and one layer of treated PDMS film (gold coated for 2.5 minutes without pre-stretching or plasma oxidation), with PDMS film at strain (%).	0	0.178	0.318	1.9
	5	0.209	0.329	1.9
	10	0.241	0.339	1.9
	15	0.272	0.350	1.9
	20	0.303	0.360	1.9
	25	0.335	0.371	1.9
	30	0.366	0.381	1.9
	35	0.384	0.396	1.9
	40	0.402	0.412	1.9
	45	0.420	0.427	1.9
	50	0.438	0.442	1.9
	55	0.456	0.458	1.9
	57	0.474	0.473	1.9

Table S01 *Material properties used in the DesignBuilder simulation*

¹Calculated from single layer properties (SHGC of 0.95 and T_{vis} of 0.95) obtained from [2]; ²Data obtained from [1]; ³Data obtained from [16]. To allow for a more valid comparison between façade assemblies, the U-value was kept consistent between the tested façades. The SHGC and T_{vis} of the façade assembly with treated PDMS film was calculated from spectrophotometry data (Section 7.1) for actuation strains 0%, 30% and 57%. These values were interpolated to estimate the other actuation strains.

Simulation parameter	Setting
Construction adjacency (Floor, ceiling, all walls except ETFE façade)	Adiabatic
Ventilation	Mechanical ventilation with heating and cooling., infiltration rate of 10 L/s - person
Heating and cooling operation	Seasonal control
	Days/week
	5
	Heating temperature
	20.0 °C
	Heating setpoint
	19.0 °C
	Cooling temperature
	22.0 °C
	Cooling setpoint
	23.0 °C
Activity	Template
	Eating/drinking area
	Occupancy
	0.2062 people/m ² , 5 days/week
Lighting	General lighting
	5.0 W/m ² - 100lux

Table S02 *Parameter settings used in the DesignBuilder simulation***Figure S18 17** *Building energy simulation*

A. A subtraction of The difference between total daily solar gains for a building with a façade with treated PDMS film from and that of a façade with infrared absorbing ETFE shows the adaptable façade ability to take advantage of higher SHGC to allow for more solar heat gain (+ Δ) (roughly 80 days during January-May and November-December) and block more solar heat gain (- Δ) the rest of the time. **B.** Hourly changes in actuation strain of a façade assembly with treated PDMS film plotted for three days of the year reflect the daily and seasonal weather variability the façade responds to by finding the optimum SHGC.

7. Building application considerations

7.1 View to the out-of-doors

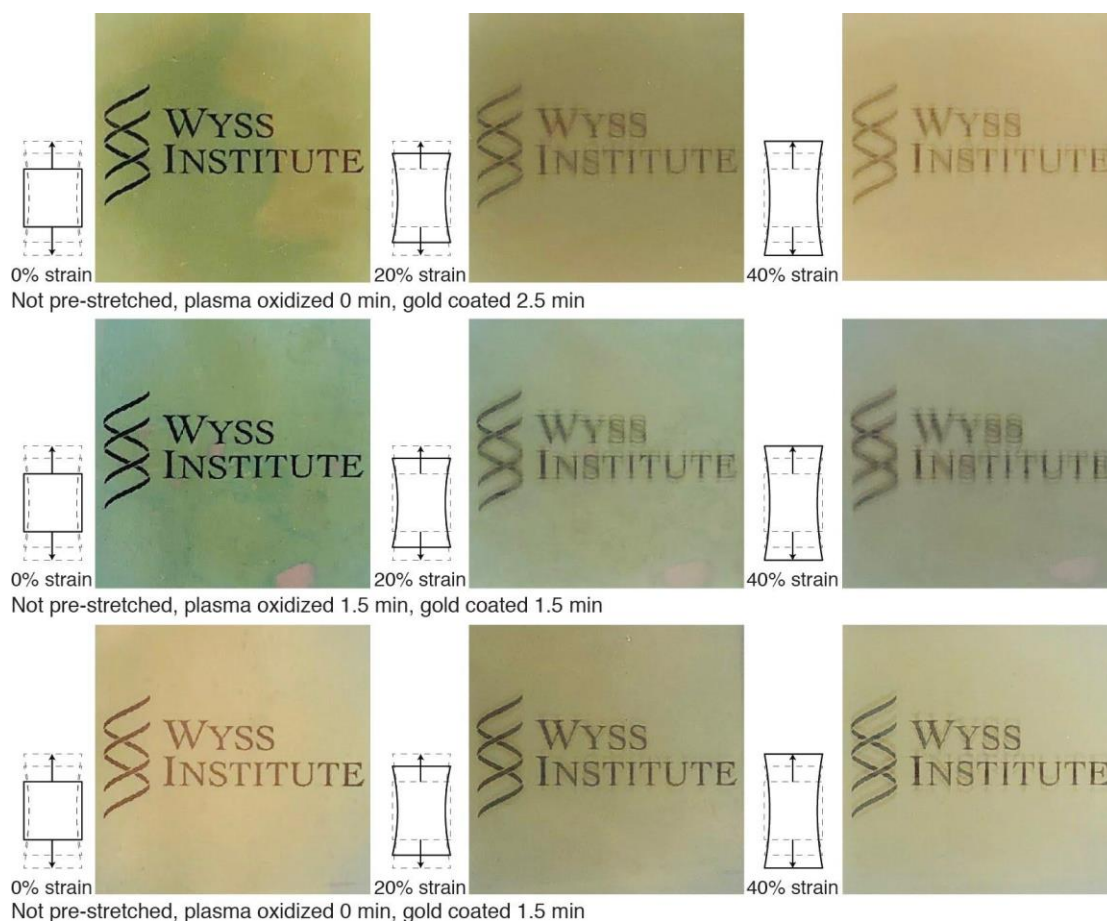


Figure S19 18 View through treated PDMS film, uniaxially actuated

Not pre-stretched, gold coated samples that include oxygen plasma treatment significantly distort the view upon actuation (middle), whereas eliminating oxygen plasma treatment reduces the level of view distortion. (top and bottom). This series of studies also shows that an increase in coating thickness (either by longer gold sputtering treatment or including plasma oxidation or both) increases view distortion upon actuation, which can be expected as a thicker rigid layer produces bigger surface cracks and more pronounced wrinkles.

7.2 Durability

The sample was mounted on a Bose ElectroForce 3200 test instrument (TA Instruments, New Castle, DE, USA) and continuously actuated uniaxially between 0% and 57% strain (a total displacement of 34.2 mm) for 10,000 cycles at 0.1Hz. Subsequently, its performance on infrared regulation was re-examined with the spectrophotometer following the process outlined in Supplemental Section 3.2. Infrared transmission changed insignificantly after continuous straining, with an average increase in weighted average T% of 0.6, -0.06, 0.32, 0.09 for strains 0%, 20%, 40%, and 57% respectively (Figure S20).

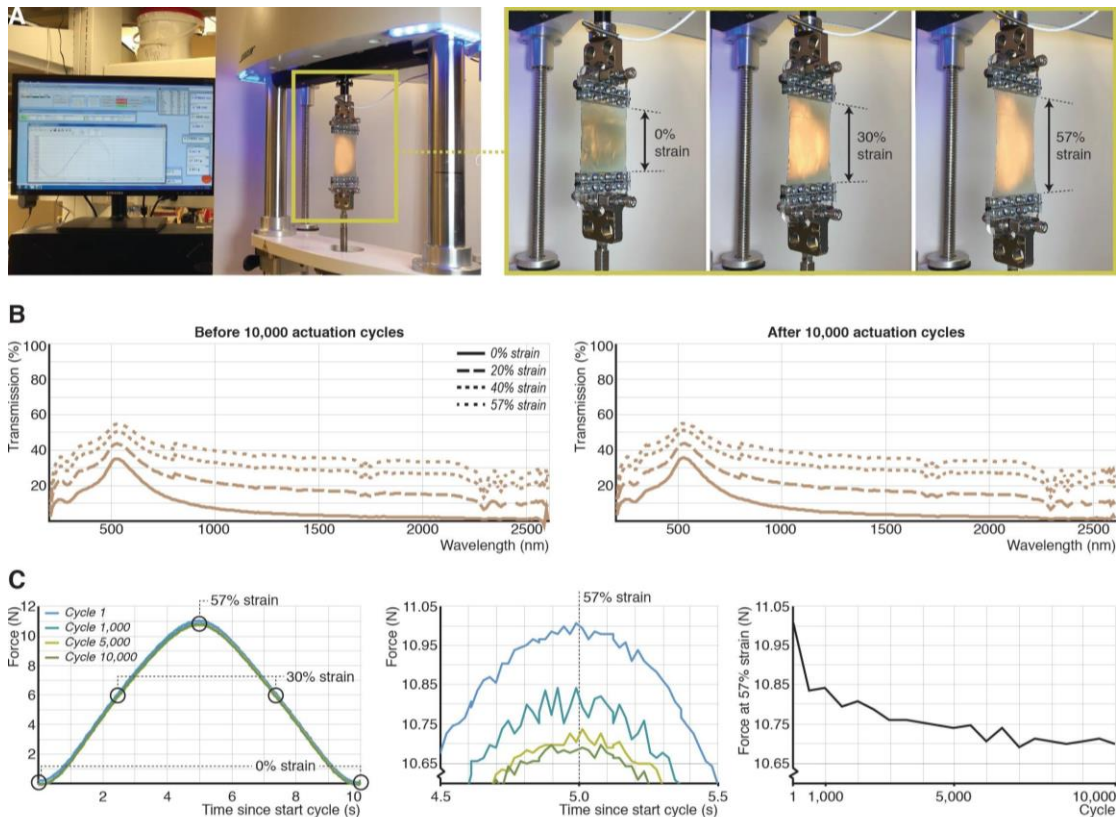


Figure S20 19 Mechanical and optical durability

A. The sample was mounted on two attachments, straining the sample with a total displacement of 34.2 mm (57% strain) for a duration of 10,000 cycles at 0.1 Hz. **B.** The sample exhibits only minor performance degradation. Infrared transmission increased insignificantly after continuous straining, with a maximum increase in $T\%$ recorded for the material at 0% strain: average of 0.57 with a standard deviation of 0.37. **C.** The material does not display significant fatigue, as the required force to actuate the material to 57% strain decreases a mere 2.8% over 10,000 cycles.

References

- [1] Nowofol, NOWOFLON ET 6235 Z-IR, n.d. <https://www.etfe-film.com/files/etfe/pdf/Product-Information-NOWOFLON-ET-6235-Z-IR.pdf> (accessed May 20, 2019).
- [2] Nowofol, Nowofol clear ETFE product information, n.d. <https://www.etfe-film.com/files/etfe/pdf/Product-Information-NOWOFLON-ET-6235-Z.pdf> (accessed May 20, 2019).
- [3] A.C.C. Rotzetter, R. Fuhrer, R.N. Grass, C.M. Schumacher, P.R. Stoessel, W.J. Stark, Micro mirror polymer composite offers mechanically switchable light transmittance, *Advanced Engineering Materials*. 16 (2014) 878–883. doi:[10.1002/adem.201300478](https://doi.org/10.1002/adem.201300478).
- [4] F. López Jiménez, S. Kumar, P. Miguel Reis, Soft color composites with tunable optical transmittance, *Advanced Optical Materials*. 4 (n.d.) 620–626. doi:[10.1002/adom.201500617](https://doi.org/10.1002/adom.201500617).
- [5] K. Hinz, J. Alvarenga, P. Kim, D. Park, J. Aizenberg, M. Bechthold, Pneumatically adaptive light modulation system (PALMS) for buildings, *Materials and Design*. 152 (2018) 156–167. doi:[10.1016/j.matdes.2018.04.044](https://doi.org/10.1016/j.matdes.2018.04.044).
- [6] J. Gao, D. Guo, S. Santhanam, G. K. Fedder. Material characterization and transfer of large-area ultra-thin polydimethylsiloxane membranes, *Journal of Microelectromechanical systems*. 24 (2015) 2170 – 2177. doi:[10.1109/JMEMS.2015.2480388](https://doi.org/10.1109/JMEMS.2015.2480388)
- [7] Standard solar spectra, (n.d.). <https://www.pveducation.org/pvcdrom/appendices/standard-solar-spectra>.
- [8] Y. Sun, Y. Wu, R. Wilson, A review of thermal and optical characterisation of complex window systems and their building performance prediction, *Applied Energy*. 222 (2018) 729–747. doi:[10.1016/j.apenergy.2018.03.144](https://doi.org/10.1016/j.apenergy.2018.03.144).

- [9] P. Kim, Y. Hu, J. Alvarenga, M. Kolle, Z. Suo, J. Aizenberg, Rational design of mechano-responsive optical materials by fine tuning the evolution of strain-dependent wrinkling patterns, *Advanced Optical Materials*. 1 (2013) 381–388. doi:[10.1002/adom.201300034](https://doi.org/10.1002/adom.201300034).
- [10] N. Bowden, W.T.S. Huck, K.E. Paul, G.M. Whitesides, The controlled formation of ordered, sinusoidal structures by plasma oxidation of an elastomeric polymer, *Applied Physics Letters*. 75 (1999) 2557. doi:[10.1063/1.125076](https://doi.org/10.1063/1.125076).
- [11] Exo-terra infrared basking spot, (n.d.). http://www.exo-terra.com/en/products/infrared_basking_spot_heating.php (accessed May 20, 2019).
- [12] R. McCluney, Suggested methodologies for determining the SHGC of complex fenestration systems for NFRC ratings, For the National Fenestration Rating Council, n.d. <https://pdfs.semanticscholar.org/972a/278727c61ccf0d86004dc350ad49188a1a2e.pdf> (accessed May 20, 2019).
- [13] A. Sharda, S. Kumar, Heat transfer through glazing systems with inter-pane shading devices: a review, *Energy Technology & Policy*. 1 (2014) 23–34. doi:[10.1080/23317000.2014.969451](https://doi.org/10.1080/23317000.2014.969451).
- [14] Sattler, ETFE-Foil structures – the flexible glass, (n.d.). <https://www.sattler-global.com/textile-architecture/etfe-foils-1013.jsp> (accessed May 20, 2019).
- [15] J.E. Mark, ed., *Polymer data handbook*, 2nd ed., Oxford University Press, New York, 2009.
- [16] Birdair, ETFE film structures, 2015. http://www.birdair.com/system/files/Birdair_ETFE_6pg_WEB.pdf (accessed May 20, 2019).